A space-time simulator for hourly wind and solar energy fields

Yash Vijay Amonkar[1], David J. Farnham[2], and Upmanu Lall[3]

[1] *UNC Institute for the Environment, UNC Chapel Hill, Chapel Hill, North Carolina, USA.*
[2] *ClimateAI, San Francisco, California, USA.*
[3] *School of Complex Adaptive Systems, Arizona State University, Tempe, Arizona, USA.*

June 23, 2024

Abstract

Spatially distributed renewable energy generation poses unique risks to power systems since the aggregate amount of energy produced in any hour depends on the spatial correlation structure of the sources. Moreover, the spatial correlation structure can vary with the time of day and season and depend on the state of the large-scale climate. These features pose a challenge for resource adequacy risk assessment using traditional statistical or machine learning methods. A new algorithm based on spatially clustered k-nearest neighbors to capture the spatio-temporal dynamics of wind and solar fields is presented and applied to data from ERCOT, Texas. The algorithm skill is analyzed both at the aggregated field level and also at the individual site level. The algorithm's utility in assessing temporally varying risks of lower-than-expected target wind and solar energy production across ERCOT is demonstrated.

Pre-print Statement:- The current version of the manuscript has not undergone peer review and is submitted as a pre-print to the EarthArXiv pre-print server.

1 Introduction

Decarbonization of electricity, electrification of large sectors of our economy, and increased penetration of renewable power sources form key pillars in combating anthropogenic climate change. The share of wind and solar based electricity generation has been increasing globally and within the United States, driven by the mandates to reduce carbon emissions [1; 2; 3; 4] and substantial reduction in their generation costs [5]. Integration of a large fraction of wind and solar based renewables into the electric grid poses numerous challenges driven by high power supply reliability requirements [6], coupled with renewable intermittency and stochasticity across multiple timescales that make their inclusion in traditional energy system models difficult [7; 8].

Resource adequacy is the ability of the grid to meet electricity demand at all locations using its supply-side and demand-side resources [9]. The 2021 Winter Storm Uri can be characterized as a supply side resource adequacy event brought about by unexpected shutdowns (lack of winterization) and abrupt increase in demand [10]. Resource adequacy assessments are a crucial component of the overall grid reliability and analyze the availability of capacity and energy to meet projected peak demand at the monthly [11], seasonal [12] and longer timescales [13]. Such assessments also include projections based on future demand and supply, along with probabilistic thermal plant failures and shutdowns [12]. The rapid rise of renewables complicates these assessments since renewables also introduce an additional weather risk [14; 15], where the built capacity might not be operational during peak hours if the wind does not blow or if it is cloudy. An additional concern is the spatio-temporal clustering of extremes across a large domain observed for drought and flood events [16; 17]. Overall, at the grid level the increasing share of wind and solar generation complicates these adequacy assessments, since such studies must account for the spatially distributed generation patterns during extreme periods.

A large fraction of electricity is sold before it is produced and consumed using the day ahead market, futures, forwards, and other power purchase agreements [18; 19]. Power producers enter into short-term (sub-daily, daily, day ahead) and long-term (weekly, seasonal, annual, or even decadal) power supply contracts to lock-in revenue at a fixed price per unit, thereby reducing their exposure to the market (electricity price) volatility [20]. The general structure of such contracts is power producers agreeing to sell a predetermined amount of power at fixed time periods for a predetermined price. Failure to meet these obligations force the power producers to buy the amount they are short on the volatile spot market, thereby incentivizing them to produce at least the amount committed. While renewable energy producers in the past relied on feed-in tariffs and other tax incentives to guarantee a steady revenue stream [21], the explosive growth of renewable capacity, maturing technologies, and low marginal costs of wind and solar power have led to the reduction of such subsidies [22]. This will eventually force renewable energy producers whose generation is intermittent and weather dependent in the same market segment with dispatchable thermal generators. Such a development would make it necessary to quantify the role of intermittency and weather variability to get accurate generation estimates and corresponding generation spreads at different time-steps to avoid overbidding. Furthermore, from the perspective of a renewable power producer with multiple generation sites spread across a grid domain, characterization of the spatially distributed generation profile helps in aggregating the risk profile and informs tail risk behavior.

The lack of long instrumental wind and solar data exacerbate the challenges associated with quantifying weather risk and resource adequacy risk posed by an ever-increasing share of renewables. [23; 24]. The finite instrumental data that encode the underlying spatiotemporal dependence can be viewed as a single sample or realization of the underlying data generating process. Given the risks posed by spatially distributed renewable electricity generation, modeling the space and time correlation structure of generation sources is crucial. This motivates research into the development of stochastic simulators or weather generators to model and generate scenarios of hourly wind and solar data across a large spatial extent.

Scenario Generators or Weather Generators, commonly used in hydroclimatic applications, are statistical models that can generate simulations of single or multiple hydroclimatic variables (e.g., streamflow, precipitations) across multiple timescales [25; 26]. They extend the data record infinitely by utilizing a statistical model that captures the underlying data generating process. It is crucial that the generative simulations accurately represent the spatiotemporal structure in the data while also expressing “innovations” which capture the possibility of diverse behaviors and trajectories. Within the energy fields, such generated simulations or synthetic realizations have applications in unit commitment and economic dispatch models, storage sizing studies, and the development of trading strategies [27; 28; 29]. The chief drawback of the current class of scenario generators is the failure to generalize to high dimensional settings (i.e., multiple sites and variables) when modeling data with spatio-temporal dependencies, with most studies restricted to 5-20 sites and variables. This failure ensures that the spatially distributed renewable energy generation risk is mischaracterized and underestimated.

Generative Adversarial Networks (GAN) [30], a class of generative models where the modeling process is a competition between two architectures, most commonly deep neural networks, have been used to model hydrometeorological variables. Studies have used GANs to generate scenarios/simulations for wind and solar farms for multiple sites [27; 31; 32], with GANs capturing the spatiotemporal characteristics but on shorter timescales of minutes to hours and for fewer sites. Similarly, diffusion probabilistic models [33], another class of generative machine learning models that work by deconstructing the data by addition of noise and relearning the data generative process have been used to simulate wind and solar fields for short time periods and a few sites [34; 35; 36].

Another broad class of models applicable to the problem of scenario generation across multiple sites are the Bayesian dynamic space-time class of models [37], which, unlike GANs and diffusion probabilistic models, are parametric with the spatial process explicitly modeled. A different approach involves the use of vector autoregressive models for joint modeling of wind, temperature, and irradiance data and Gaussian copulas for streamflow simulation [38]. The simulation of energy (wind-solar) fields must be accomplished at the regional level to model the spatial risk, thereby making it a high-dimensional problem; consequently, any approach must be able to scale to high dimensions, motivating algorithm development.

Literature analyzing wind and solar intermittency is focused on the sub-daily and sub-hourly time scale with a focus on understanding the role of batteries in meeting shortages at these time scales, where on the other hand, climate risk literature analyzing future climate risk is dominated by global climate model (GCM) projections up to 2100 without robust consideration of the underlying biases and uncertainties in local wind and solar variables [39; 40; 41]. Consequently, tools are necessary that can help bridge the divide between these approaches by including spatiotemporal patterns of climate-induced risk for renewable energy systems with a temporal granularity at the hourly scale but with data availability across multiple years using observed and validated data records.

The primary objective of this study is the development and presentation of a novel k-nearest neighbors based generative algorithm that can model and simulate the joint hourly wind and solar data across a large spatial domain. The k-nearest neighbors (KNN) algorithm is one of the earliest machine learning based algorithms used for regression and forecasting [42; 43; 44]. Lall and Sharma (1996) [45] and Rajagopalan and Lall (1998) [46] first used KNN in a simulation mode, applying them to a single and five hydroclimatic fields respectively. Amonkar et al. (2022) [47] using the k-nearest neighbors space time simulation (KSTS) algorithm extended KNN's simulation capability to hundreds of dimensions with applications demonstrated to daily wind and solar fields across ERCOT. The algorithm presented in this study extends the KSTS algorithm [47] by considering clustered heterogeneities in the spatial dependence structure, allowing it to model more complex spatio-temporal data.

The general structure of the proposed clustering based k-nearest neighbor space-time simulator (CKSTS) algorithm is presented here. The CKSTS first includes a k-nearest neighbors model for the temporal variability at each site and across each variable type (wind and solar). A state space of the time dynamics is defined through an embedding of the underlying univariate time series [48; 49]. A probabilistic similarity metric is applied to the time indices for each series to derive a group similarity measure in time. A generative model for time series simulation is developed by randomly drawing from the group level k-nearest neighbors of the embedding at each time step [45]. The spatial dependence structure is preserved by identifying the most likely time neighbors for the group based on the aggregated neighbor likelihoods across the sites and variables. Given that wind-solar fields exhibit heterogeneity across and within fields across distances [47], the algorithm utilizes a clustering sub-module to identify sub-groups of wind and solar sites that exhibit similar spatio-temporal evolution dynamics as measured by the similarities in their identified nearest neighbors. The KSTS algorithm includes spatial dependence by aggregating neighbor likelihoods for the entire spatial field. The CKSTS algorithm includes an additional clustering step that models the spatial dependence by aggregating neighbor likelihoods for sub-regions (or clusters) separately across the spatial field. Clustering is carried out on the neighbor likelihoods at each time step for all sites and variables to identify the separate sub-regions. Consequently, the KSTS algorithm can be viewed as a special case of the CKSTS algorithm that assumes the spatial dependence can be modeled by a single cluster (i.e., aggregating the neighbor likelihoods across the entire spatial domain).

The Electric Reliability Council of Texas (ERCOT), is one of the three main grids within the contiguous United States and manages about 90% of Texas's electric load [50]. Furthermore, Texas and ERCOT lead the nation in wind and solar installations and generation [51]. Additionally, ERCOT and Texas are characterized by a rapid development and change in the mix of renewables, with the installed capacity ratio between wind and solar moving from 10:1 a few years ago to 3:1 today and is projected to be 1:1 in the near future [52]. Such rapid changes necessitate joint modeling of both wind and solar fields. In this study, hourly wind and solar data over ERCOT are used as a case study to study the skill of the CKSTS algorithm in modeling the spatio-temporal data. They are then compared against the simulations from the KSTS algorithm that serve as a comparative model. Finally, simulations developed using the KNN algorithm are also used for comparison as a baseline case when no spatial structure or information is considered.

Overall, this study presents the clustering-based k-nearest neighbor space-time simulator (CKSTS) algorithm with an application to ERCOT that demonstrates the ability to model joint wind and solar fields at an hourly timescale. Section 2 includes a description of the data used in the study, while section 3 presents the CKSTS algorithm along with details on hyperparameter selection. The simulation skill assessment of the generated simulations using the CKSTS algorithm is shown in section 4 along with comparisons from the simulations generated with KNN and KSTS algorithms. The conclusion and discussion of the next steps are presented in section 5.

2 Data

2.1 Wind and solar data

The ERA-5 reanalysis dataset is used as the source of wind and solar fields [53]. The two variables considered are wind speed (m/s) at 100 meters and downward surface solar radiation (W/m^2).

The CKSTS algorithm is used to simulate the wind speeds and downward surface solar radiation. Henceforth, we refer to wind speeds and downward surface solar radiation as wind and solar, respectively, unless otherwise specified. The variables are at an hourly resolution and span 5 years from January 1, 2018, to December 31, 2022, with a total of 43824 time-steps. The spatial resolution of the data is set at $0.5^o \times 0.5^o$ latitude-longitude, with a total of 216 grid points across the Texas Interconnection, which is also referred to as the Electric Reliability Council of Texas (ERCOT) (Figure 1).

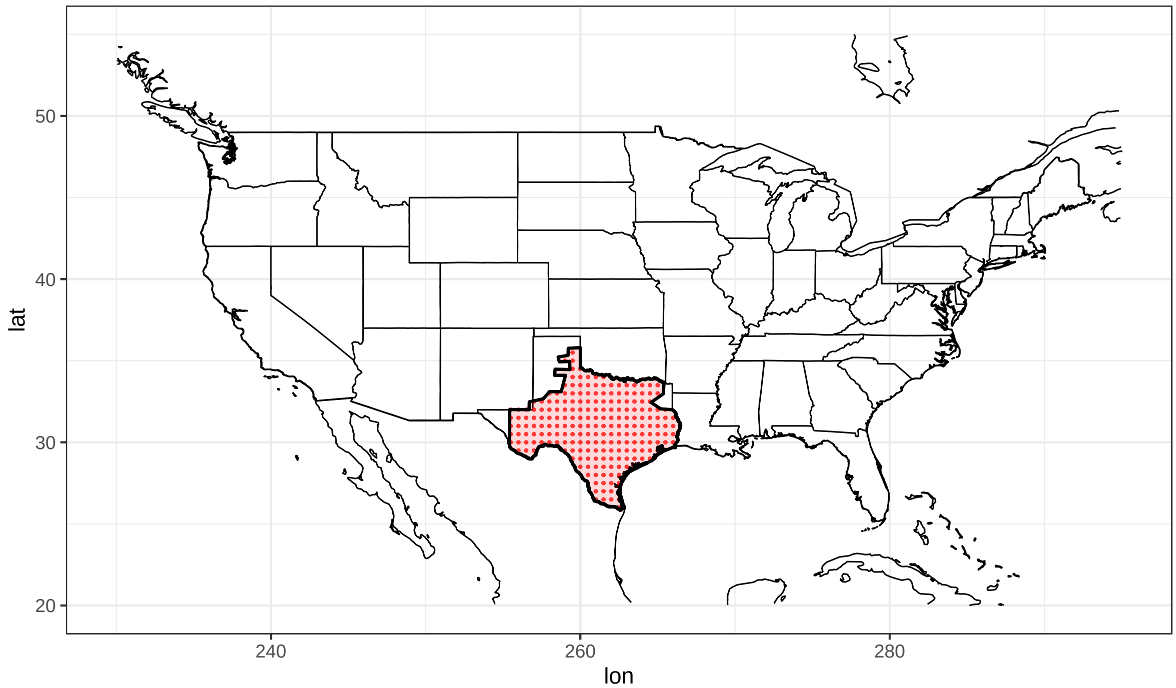

Figure 1: ERCOT domain plot - The red-shaded region denotes the area administered by ERCOT. The red dots (216) are the locations of the grid points ($0.5°$ lat $\times$ $0.5°$ lon) from the ERA-5 reanalysis dataset.

2.2 Wind and Solar Installations

The locations of the installed commercial scale wind and solar power generators (as of 2022) are taken from the U.S. Energy Information Administration's Form EIA-860 that collects generator-level specific information about existing and planned generators [51]. The Form EIA-860 is a comprehensive source of geospatial data on energy infrastructure and resources within the United States. All power plants with over 1 MW of installed boilerplate capacity are included in the dataset. The hourly power generation at the wind and solar power generators is computed using the hourly wind speeds and downward surface solar radiation from the grid point closest to the generator location. The total installed wind capacity within ERCOT is 35965 MW, whereas 11354 MW of solar generation is installed within ERCOT.

Two capacity allocation scenarios considered are 'Uniform Capacity' allocation and 'Installed Capacity' allocation (Figure 2). The 'Installed Capacity' allocation refers to operable wind and solar electric generating capacity within the ERCOT region and is taken from the US EIA dataset

[51]. The ‘Uniform Capacity’ allocation scenario is where the total wind and solar capacity across ERCOT from the previous scenario is equally divided among the grid points in the ERCOT region, respectively. The scenarios allow for the CKSTS simulation skill tests of the aggregate production (uniform capacity allocation) and production in a spatial subdivision of interest (installed capacity allocation).

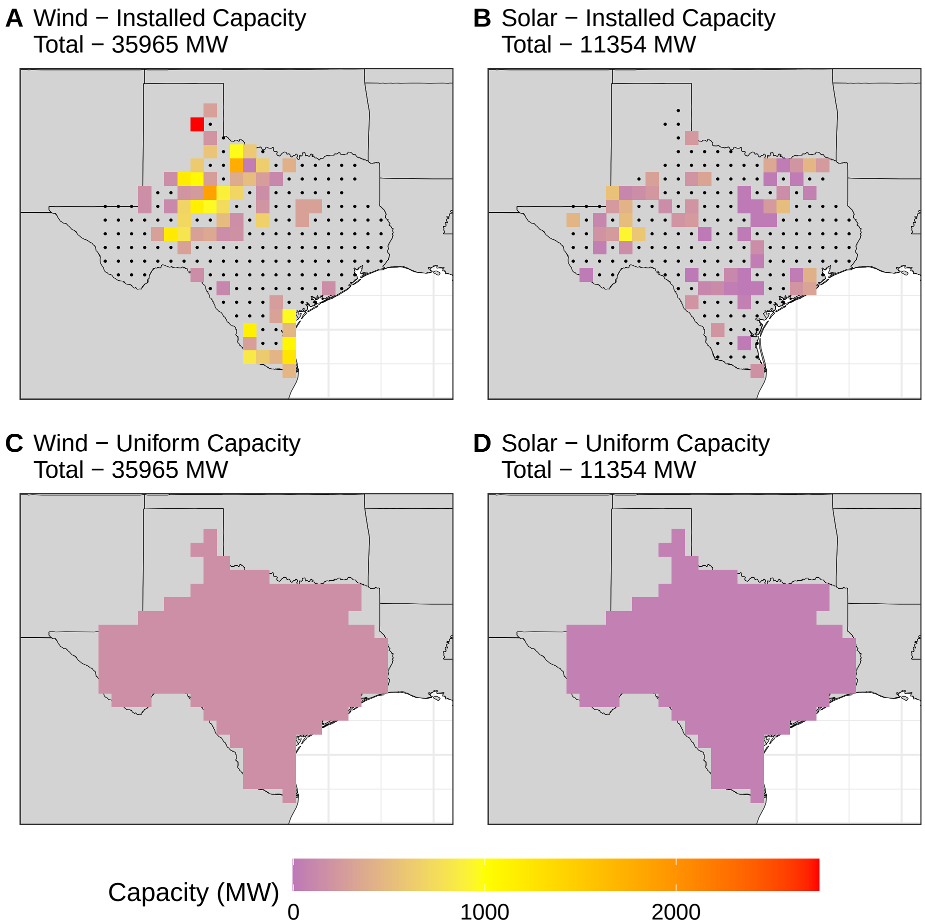

Figure 2: The capacity allocation scenarios considered are (top row) Installed capacity allocation scenario, and (bottom row) Uniform capacity allocation scenario. (A & C) Wind. (B & D) Solar. For both scenarios, wind and solar have a total installed capacity of 35965 MW and 11354 MW, respectively. The regions with small black dots denote grid points where no wind and solar capacity is allocated/exists.

2.3 Wind and Solar Power Calculations

Wind speeds are converted to wind capacity factors using the turbine power curve from a V90 Vestas turbine (Figure S1). Downward surface solar radiation is converted to the solar capacity factor using the relationship provided in Bett and Thornton [54], without accounting for temperature dependence. The computed wind and solar capacity factors at each grid point are converted into wind and solar power by multiplication with the wind and solar capacity allocated at that grid point for the uniform and installed capacity allocation scenarios.

3 Methods

3.1 Clustering-based k-nearest neighbors space-time simulator (CKSTS) algorithm

The general structure and the steps of the CKSTS algorithm are provided below, while the schematic example application of the CKSTS algorithm is shown in Figure 3.

Step 1: Define the composition of the state space $D_{i,t}$.

Define a state space $D_{i,t}$ of dimension m which is the number of embedding delay lags. The state space can be a single lag, multiple lags and/or disjoint lags allowing for custom time dependencies. The embedding selected for the simulator application could be,

Case 1 $D_{i,t}$:- (x_{t-1}, x_{t-2}); m = 2
Case 2 $D_{i,t}$:- ($x_{t-\tau}$, $x_{t-2\tau}$, $x_{t-\phi}$, $x_{t-2\phi}$); m = 4, $\tau = 1$, $\phi = 12$
Case 3 $D_{i,t}$:- (x_{t-1}, x_{t-4} x_{t-7}); m = 3

The first case represents dependence on the previous two values. The second case represents a state space dependence on the last two values and the values 12 and 24 steps before the current value, allowing for incorporation of annual cycle in monthly data. The state space $D_{i,t}$ is defined for each site/variable i and the current time t, whereas $D_{i,T}$ are all the historic vectors which correspond to the selected embedding structure for site i.

Step 2:- Compute the k-nearest neighbors for each site at time t.

At time step t and site/variable i using the current state space vector $D_{i,t}$, identify the k-nearest neighbors in the historical data using the weighted Euclidean distance measure,

$$r_{i,t} = \left(\sum_{j=1}^{m} w_j([D_{i,t}]_j - [D_{i,T}]_j)^2 \right)^{1/2}$$

where, $[D_{i,t}]_j$ and $[D_{i,T}]_j$ are the j^{th} components of $D_{i,t}$ and $D_{i,T}$ respectively and w_j are the weights assigned to each of the embedding lags. This is repeated for all sites. The ordered set of time indices which correspond to the *k* nearest neighbors (as defined by the Euclidean distances stored in $r_{i,t}$) of site *i* at time *t* are stored in $\tau_{i,t}$. We use uniform weights w_j in the applications presented here, but an optimization of these weights could be considered.

Step 3:- Compute resampling probabilities for k nearest neighbor indices using a discrete kernel p_j at each site.

$$p_j = \frac{1/j}{\sum_{j=1}^{k} 1/j}$$

where p_j is the resampling probability for the jth element (time instance of the jth nearest neighbor of $D_{i,t}$) in $\tau_{i,t}$. The resampling kernel stays the same across all time *t* and across all sites, and is pre-computed and stored prior to simulation. It is a function of the number of neighbors *k* and not the distances.

Step 4:- Define $V_{i,t}$ for time t.

Define $V_{i,t}$ as a matrix where the rows and columns correspond to the sites/variables and unique time indices from the historical data, respectively. The columns record the resampling probabilities p_k associated with each historical time index corresponding to the k-nearest neighbors of each site/variable i. Time indices that do not correspond to a k-nearest neighbor get a value of 0. If two series have an identical set of time indices as their k-nearest neighbors, then their dynamics are perfectly correlated. Thus, the clustering on the resampling probabilities of the k-nearest neighbors of the series at each time step recognizes the similarity in the temporal dynamics at that time - and hence recognizes the local similarity in the dynamics rather than the global correlation structure of the series.

Step 5:- Clustering on $V_{i,t}$ at time t

Clustering is now carried out on $V_{i,t}$ to identify sites which have similar state-space evolution dynamics, as represented by similarity in the nearest neighbor likelihoods and resampling probabilities. We use hierarchical clustering with Calinski-Harabasz (CH) index [55] to select the optimum number of clusters, which is not known a priori. If the optimum number of clusters selected using the CH index is c, $V_{i,t}$ is then divided into c separate matrices based on cluster memberships as follows,

$$V_{clust} = V_{n_j,t}$$

where V_{clust} contains the n_j individual sites/grids which belong to cluster j. Each site is assigned to one cluster such that the number of cluster members n_j across all clusters c adds up to the total number of sites s.

$$\sum_{j=1}^{c} n_j = s$$

Step 6:- Compute the similarity vector S_t separately for all clusters.

We compute similarity vectors for individual clusters separately. The similarity vector S_t is defined as the sum of all elements in each column in V_{clust}.

$$S_t = \sum_{i=1}^{n_j} V_{clust_{i,t}}$$

where, n_j is the number of sites in cluster j. This is repeated for all clusters.

Step 7:- Curtail and scale the similarity vector S_t separately for all clusters.

The similarity vectors S_t for all clusters c are ordered and curtailed to their highest k values, respectively. The time indices associated with the k highest values of S_t are selected as the k-nearest neighbor candidates for the all the sites in their respective cluster. The probabilities of the associated k neighbors are rescaled to add up to 1.

$$S_t = \frac{S_t}{\sum S_t}$$

This operation is repeated for all similarity vectors.

Step 8:- Re-sample the full spatial field for time $t + 1$ using similarity vectors S_t.

Using the discrete probability mass function S_t, sample a single value for the sites in that cluster. Repeat the procedure for all clusters, which re-samples the entire field across all sites. These selected values correspond to simulated data for time step $t + 1$. Return to Step 2 if further time-steps are needed for the simulation.

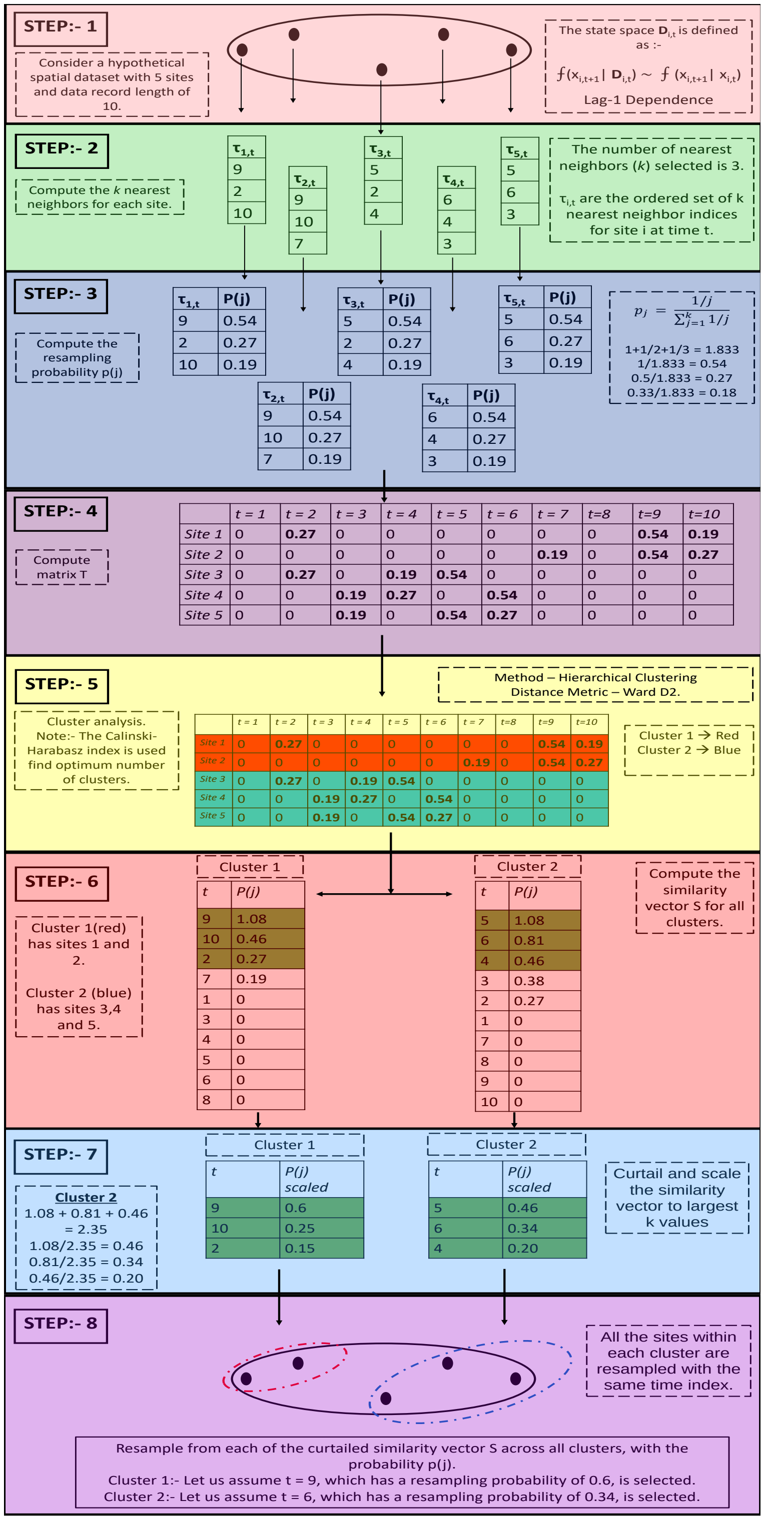

Figure 3: Example application of the CKSTS algorithm to a spatial dataset consisting of 5 grids/sites and data record (time) length of 10.

3.2 Algorithm hyper-parameters

3.2.1 Clustering based hyper-parameters

Overall Method - Since the cluster labels are not known a priori, an unsupervised learning algorithm is required. While it could be postulated that the chief difference between clusters is the variable type i.e., wind and solar, this assumes that the internal dynamics within fields are homogeneous, which is not the case and is the primary motivation in developing the CKSTS algorithm. The main choices for unsupervised clustering algorithms are between the k-means clustering [56] and agglomerative hierarchical clustering [57], both of which are widely used. The primary advantage of k-means clustering is the lower computational cost, while hierarchical clustering requires the computation and storage of the $n \times n$ dissimilarity matrix, making it expensive as the dataset grows. The n of the clustering matrix for our application is $432 \times k'$, with k' being the number of unique neighbor indices, which is generally ~ 50. Inversion of this matrix size is feasible, and the computational disadvantage of the hierarchical clustering is not a hindrance.

For hierarchical clustering, once a linkage method is selected, the clustering results are fixed (i.e., the resulting dendrogram remains static, and the cluster labels are stable), giving stable results. On the other hand, minimizing the objective function of the k-means algorithm is a NP-hard problem [58]. Further, the k-means clustering algorithm converges to a local minima and only converges to the global minimum when the clusters are well separated [59; 60]. Thus, in practice, k-means requires multiple random initializations and selection of the solution with the lowest sum of squared errors. Overall, k-means clustering works well when the clusters are spherical/elliptical in shape, compact, and well separated. The high dimensionality and sparsity of the nearest neighbor likelihoods make application of the k-means clustering difficult. Consequently, the agglomerative hierarchical clustering algorithm is selected as the clustering method for the application to wind and solar fields across ERCOT. The basic steps of the clustering algorithm are as follows:-

Step 1:- Assume all n data points are individual clusters with a total of n clusters.
Step 2:- Compute the dissimilarity matrix between all clusters.
Step 3:- Merge the two most similar clusters based on the computed dissimilarities.
Step 4:- Repeat steps 2 and 3 until a single cluster is left.

The outcome of this algorithm can be visually displayed by a tree like structure called a dendrogram. Hierarchical clustering itself has many hyperparameters, which are covered below.

Distances - The hierarchical clustering relies on the dissimilarity matrix of the clusters, which requires a method to compute the distances between them. The Euclidean distance metric is generally used to calculate distances between clusters. Other options are Mahalanobis distance metric, Manhattan (L_1) distance metric, and Itakura-Saito distance metric [61].

Linkage methods - The linkage method is used at every iteration to identify the two most similar clusters and merge them. The choices of linkage methods include Single, Complete, Average, Centroid, Median, and Ward's method. Ward's method [62] creates groups such that variance is minimized within clusters. It is less susceptible to noise and outliers and is biased towards globular clusters. Murtagh and Legendre [63] provide a comparative analysis of Ward's method and similar implementations across the literature.

Number of clusters - This is the most crucial hyperparameter for the clustering algorithm. Since squared errors (within cluster variance) reduce with increasing the number of clusters (reducing to zero when number of clusters equals number of data points), minimization can be carried out for a fixed number of clusters. The best possible outcome for selection is the presence of prior domain knowledge, for example, if it is known a priori that the population is drawn from three different distributions, the number of clusters would be specified as three. This is not the case for the current application, and validation metrics are needed to select the number of clusters.

The Calinski-Harabasz Index (CH Index) [55] is used to select the number of clusters. The CH index, also called the variance ratio criterion, is one of the most efficient methods in finding the number of clusters [64]. The index is computed as follows:-

$$CH = \frac{\sum_{k=1}^{NC} n_k \times d(c_k, c)}{NC - 1} / \frac{\sum_{k=1}^{NC} \sum_{i=1}^{n_k} d(d_i, c_k)}{N - NC}$$

where, N and NC are the number of data points and clusters respectively, c_k is the centroid of cluster k and c is the global centroid, n_k is the number of elements in cluster k and d(x,y) denotes the Euclidean distance between points x and y. The number of clusters with the maximum value of the CH index is selected, with higher values denoting dense and well-separated clusters.

Silhouette analysis [65] can also be used to select the number of clusters. The silhouette score checks for internal cohesion within cluster data points and how well these points are separated from other clusters. The score ranges from -1 to +1, with higher values indicating better internal cohesion and external separation. The elbow method can also be used as a heuristic, where a kink or drop (elbow) in the curve of the plotted within-cluster sum of squares vs. number of clusters is taken as the number of clusters for the algorithm [66]. Other options to select and validate the number of clusters include Dunn's indices [67], Davies-Bouldin index [68], Xie-Beni index [69] and I index [70]. The application presented in the following section used the Calinski-Harabasz (CH) index to select the number of clusters at each time step.

We refer the reader to the supplemental materials section for details on the algorithm hyperparameter selection for the resampling kernel (p_j), number of neighbors (k), model order (m), and scaling weights (w).

4 Results

The CKSTS algorithm was used to generate 48 independent realizations of the same length as the data (5 years (2018-2022) or 43824 hours) for the joint wind-solar fields across ERCOT. The algorithm used a lag-1 dependence model with a 15-day moving window to capture the seasonality in both fields. The KSTS and the KNN algorithms were also used to generate 48 independent separate realizations of the data and serve as baseline comparison models. The next subsections include the analysis of the ability of the CKSTS algorithm to reproduce the spatiotemporal characteristics of the joint hourly wind-solar data within and across fields, the model limitations, along with the advantages compared to the KSTS and KNN models.

4.1 CKSTS reproduces the field properties

The CKSTS algorithm simulates hourly wind and solar data across all 216 sites across ERCOT. The simulation skill of the algorithm in capturing the dynamics of the overall behavior of wind and solar across the entire region is analyzed first. The time series for each field is computed by averaging the individual time series across all sites.

The ability of the CKSTS algorithm to capture the overall field data density distribution is first analyzed. Figure 4 shows the kernel density estimate of the probability desity function of the spatially averaged (A) wind speeds and (B) downward surface solar radiation across ERCOT. The red and black lines in both sub-plots denote the reanalysis data and the simulation's median density. The gray region denotes the 5th-95th percentile range spread in the generated simulations. The solar density distribution is highly non-normal due to the diurnal cycle, imparting a unique density form that the CKSTS algorithm is able to reproduce. Furthermore, the data density in the generated simulations is representative of the underlying distribution in the reanalysis data, highlighting that the CKSTS algorithm is also capable of modeling the wind data distribution. For both fields, CKSTS captures the different data density distribution characteristics in the mean and extremities of the spatially averaged fields, which are of interest from the perspective of the total energy generated under spatial dependence.

The ability of the CKSTS algorithm to model the auto-correlation in the wind and solar fields is displayed in Figure 5. Figure 5 denotes the auto-correlation function (ACF) for hourly lags up to 25 hours for both wind and solar fields. The generated simulations for wind are characterized by a small bias, with simulations consistently underestimating the data ACF, with the bias decreasing over a lag of 12 hours. Overall, the magnitude of the bias seems to be constant in the first few hours, and the generated simulations capture the trend in the ACF at the daily level. The solar simulations are representative of the underlying solar ACF structure (and characterized by very-low spread) with no bias as seen in the wind field.

Principal Component Analysis is a non-parametric dimension reduction method that helps analyze the spatiotemporal structure of the data without explicitly specifying the underlying structure a priori [71]. The principal components (PC) are the identified modes of variability of the data and are ordered based on their corresponding eigenvalues, i.e., variance explained. Figure S2 shows the eigenvectors and the eigenvalues of the leading principal components for both the data and simulations. The first principal component of the wind field explains 50% and 51% of the total variance in the data and generated simulations, respectively. Further, the eigenvectors associated with that PC also denote similar patterns across ERCOT. Similarly, the first and second PCs of the solar field from both the data and simulations explain 94% and 2% of the total variance for both the data and simulations, respectively. The eigenvectors of both PCs from the data and simulations also represent similar spatial patterns. Overall, Figure S2 shows that the CKSTS algorithm is able to capture the overall spatiotemporal characteristics with little bias across both wind and solar fields spanning the entirety of ERCOT.

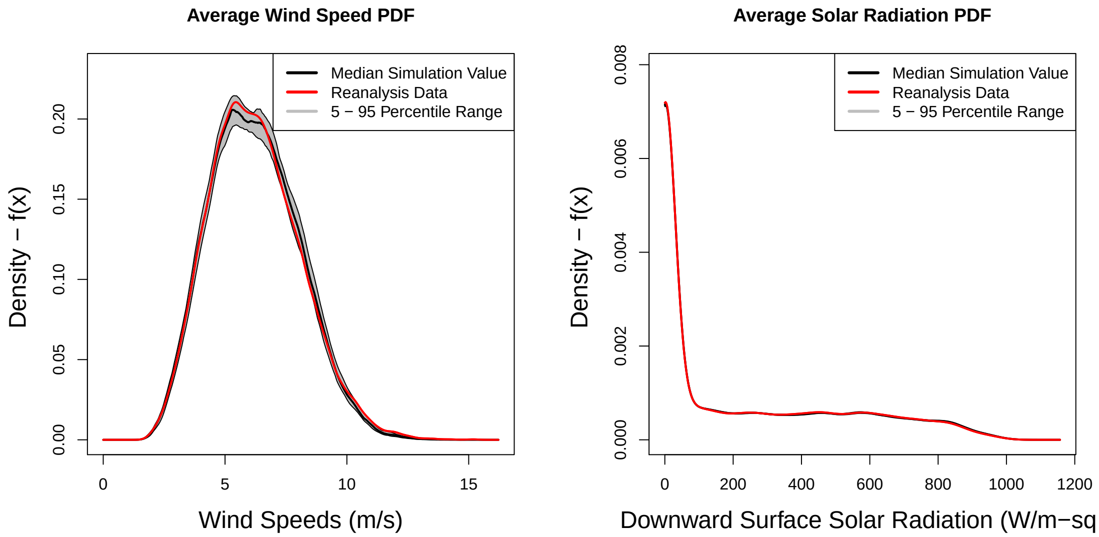

Figure 4: Probability density function (PDF) of the individual fields across ERCOT. The red and black lines denote the reanalysis data and median simulation probability density function. The grey region is the mid-90th (5th-95th) percentile range of the simulation spread. (Left) Wind. (Right) Solar.

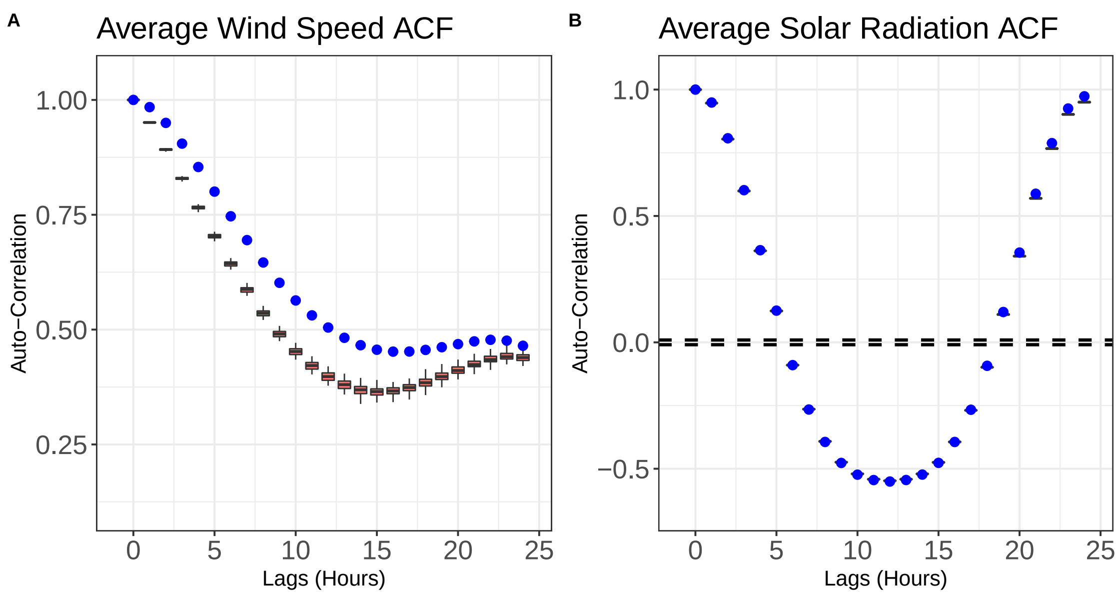

Figure 5: Auto-correlation for hourly lags for the (A) wind and (B) solar fields. The blue dots denote the autocorrelation in the reanalysis dataset. The boxplots denote the spread in the ACF within the generated simulations. The dotted black lines denote thresholds for the significance of the auto-correlations values.

4.2 CKSTS reproduces the cross-field correlation structure

The skill of the CKSTS algorithm in representing the cross-field correlation between wind and solar at the individual grid-cell level is analyzed in this subsection. Overall, the correlation between hourly wind and solar is non-homogeneous, being negative across large parts of ERCOT and positive in a small portion inland (Figure 6). The CKSTS generated simulations capture this correlation structure with little to no bias (Figure 6). Furthermore, the changing seasonal correlation structure between wind and solar across ERCOT is also well represented in the CKSTS generated simulations (Figure 7).

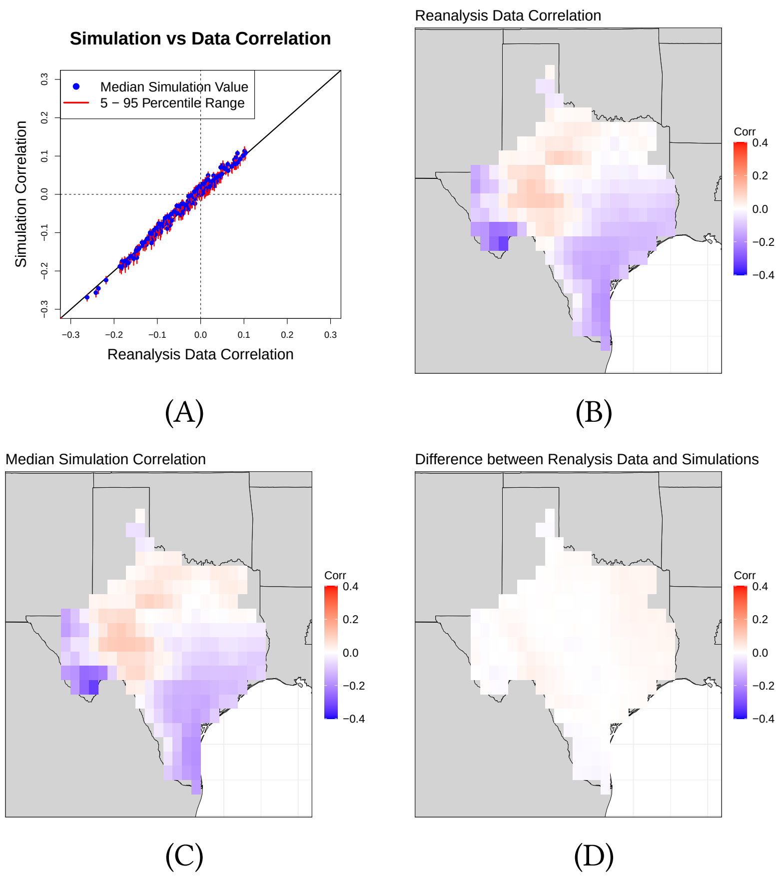

Figure 6: Pearson correlation between wind and solar at each grid point based on simultaneous simulations of wind and solar using CKSTS. (A) Simulation correlation vs. reanalysis data correlation between wind and solar, where the red lines denote the mid-90th (5th-95th) percentile range and the blue dots denote the median value in the simulation spread. (B) Map of the grid-wise correlations in the reanalysis data record. (C) Map of the grids median simulation correlations. (D) Map of the difference between (B) and (C).

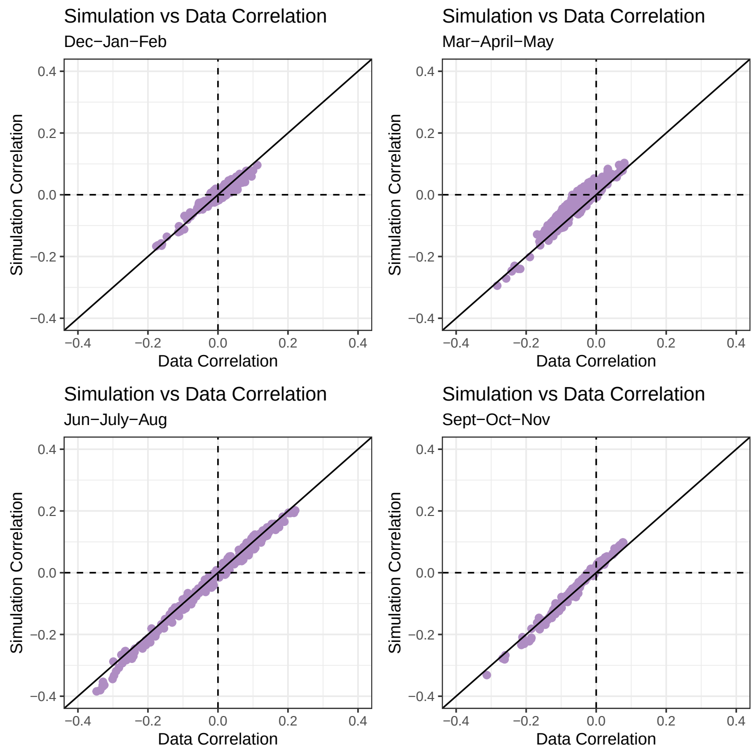

Figure 7: Seasonal simulation vs. data correlation between wind and solar at each grid point for CKSTS simulations. (A) Dec-Jan-Feb. (B) Mar-Apr-May. (C) Jun-Jul-Aug. (D) Sep-Oct-Nov.

4.3 CKSTS reproduces the individual site characteristics

The simulation skill of the CKSTS algorithm in capturing the underlying spatiotemporal characteristics at the site-level is analyzed in this subsection. The simulations from the CKSTS algorithm reproduce the mean, standard deviation, minimum, and maximum across sites for both wind and solar fields (Figure S3). Further, the spatial correlation within a field, for example, the correlation between wind speeds at two sites across Texas, is well represented by the CKSTS generated simulations (Figure S4). The auto-correlation in the generated simulations for wind speeds at the site level is characterized by a small bias (Figure S5 (A) and Figure S6 (A)), which reduces as we increase the hourly lags. The algorithm simulations capture the auto-correlation for solar radiation without any bias (Figure S5 (B) and Figure S6 (B)). The CKSTS algorithm generated simulations also skillfully represent without any bias the density distribution (Figure S7), quantiles (Figure S8 and Figure S9), daily cycle (Figure S10), and seasonality (Figure S11).

4.4 Comparison to other models

This subsection analyzes and compares the CKSTS algorithm skill with the KSTS and the KNN algorithm skill. All three algorithms capture the spatio-temporal variability across wind and solar at the site level. Furthermore, the simulation skill between CKSTS and KSTS is almost similar for aggregated (field-level) solar metrics, but given that the installed wind capacity is about 3 times higher in ERCOT (Figure 2), high simulation fidelity for wind is crucial, and consequently the simulation skill for the wind field with a focus on aggregated metrics across ERCOT is analyzed in this subsection. This helps analyze the ability of each model to capture the spatially distributed wind generation variability across ERCOT.

Figure 8 displays the ACF of the aggregate wind speeds across ERCOT for (A) CKSTS, (B) KSTS and (C) KNN model simulations, with the blue dots denoting the data ACF and the boxplots the spread in the ACF across the generated simulations. Figure 9 displays the spread (5th-95th percentile) in the total wind hourly production for the installed capacity scenario across ERCOT in MWh across the (A) CKSTS, (B) KSTS and (C) KNN simulations. Figure 10 displays the scatter plot between the observed and simulated spatial cross-correlation for a subset of wind sites across ERCOT.

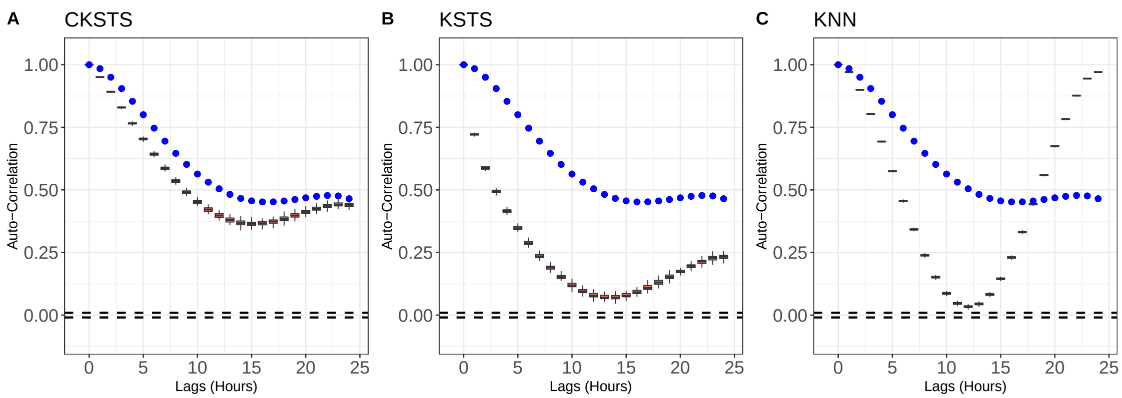

Figure 8: Auto-correlation for hourly lags for the wind field across (A) CKSTS and (B) KSTS (C) KNN models. The blue dots denote the autocorrelation in the reanalysis dataset. The boxplots denote the spread in the ACF within the generated simulations. The dotted black lines denote thresholds for the significance of the auto-correlations values.

The CKSTS simulations are first compared with the KSTS simulations. The ability of CKSTS (Figure 8 (A)) to represent the auto-correlation structure at the aggregated domain is far better with just a small underestimation when compared to the KSTS based simulations (Figure 8 (B)) which have a much larger bias in capturing this aggregated data metric. Model simulations from both are similar to the total reanalysis data generation within ERCOT, but CKSTS does a better job at capturing this aggregated metric when compared to the KSTS which has a slight under-estimation of the lower production values and over-estimation of the higher production values (Figure 9 (A) and (B)). Since both CKSTS and KSTS models explicitly include considerations of the spatial dimensions of the data, they faithfully represent the cross-correlation structure, with CKSTS exhibiting greater variability when compared to KSTS (Figure 10 (A) and (B)).

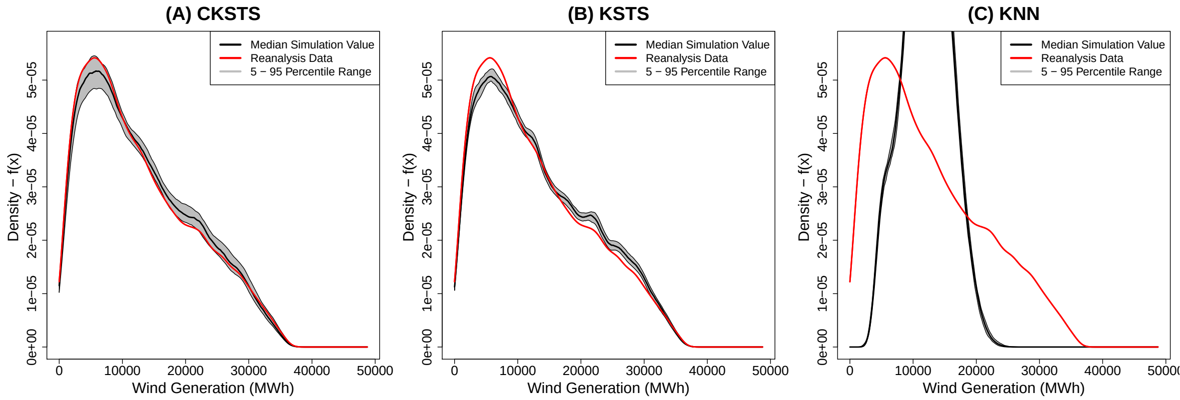

Figure 9: Probability density function (PDF) plots for the total wind generated power under the installed scenario (Figure 2) across ERCOT for (A) CKSTS, (B) KSTS, and (C) KNN. The red line denotes the reanalysis data probability density function and the black line denotes the median simulation density. The grey region is the mid 90th (5th - 95th) percentile range of the simulation spread.

Figure 8 (C) and Figure 9 (C) show that the KNN model can capture neither the underlying auto-correlation nor overall production profile at the domain level, with extremely large deviations from the underlying data characteristics. The cause of this total lack of skill is displayed in Figure 10 (C) and can be attributed to the non-inclusion of any spatial consideration within the model. Overall, since the KNN algorithm models each wind and solar site individually, without any consideration of the underlying spatial structure, this causes KNN based simulations to completely fail in modeling any spatially aggregated property of either the wind or the solar field in spite of having good skill at the site level.

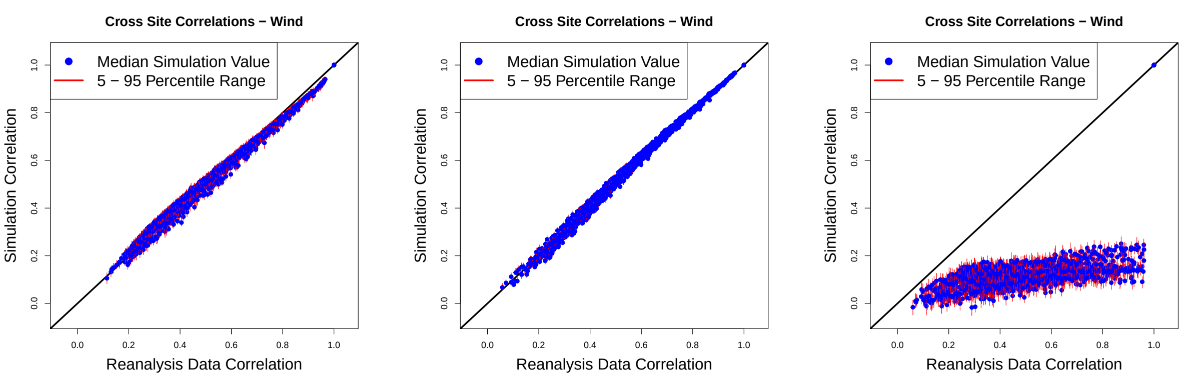

(A) CKSTS (B) KSTS (C) KNN

Figure 10: Simulation vs. reanalysis data cross site correlation for the wind field. (A) CKSTS.(B) KSTS (C) KNN. 40 grids out of 216 are randomly selected and the 40 x 40 cross correlation values are computed and plotted instead of the entire 216 x 216 correlation values. The correlations are computed using Pearson's method. The red lines denote the mid 90th(5th-95th) percentile range, and the blue dots denote the median value in the simulation spread.

Overall, both CKSTS and KSTS generated simulation exhibit near equal skill in capturing the underlying spatially aggregated metrics while also modeling all metrics of interest at the individual site level. This is not surprising since the KSTS can be thought of as a special case of the CKSTS where the number of clusters are assumed to be 1. The only exception is modeling the auto-correlation structure, where KSTS severely underestimates the correlation at the hourly level. The KNN which includes no consideration of the spatial modeling fails at replicating any of the aggregated metrics even though the simulation skill is high at the site-level. Overall, the CKSTS algorithm works well in modelling spatio-temporally complex data like hourly wind and solar across ERCOT.

4.5 Power production profiles and short-term agreements

In this section, the skill of the CKSTS algorithm in facilitating uncertainty estimation given a limited data record for short-term (sub-daily) power supply contracts is analyzed. This simplified example serves as an additional simulation skill assessment of the spatially distributed generation. Amonkar et al. [47] define supply-side energy droughts as a continuous period where the cumulative power production falls below a target threshold. The target threshold at the daily timescale can change every calendar day and be considered a forward contract's daily obligation, which varies based on seasonality, thereby at least partially accounting for the weather variability. At the hourly resolution, power producers are exposed to further intermittency causing deficits, which can lead to lower generation below the pre-specified supply commitments, thereby incurring penalties. In this section, we analyze the skill of the CKSTS algorithm in capturing the distribution of the power production profiles and, consequently, deficits at an aggregate level over ERCOT.

This simplified analysis is focused on power supply contracts over the sub-daily timescales. Such contracts, while not common, are one way for renewable energy producers to enter the bidding process once the feed-in incentives reduce. These contracts can also be contextualized as power purchase agreements, where the power delivery targets vary depending on the seasonality. The three parameters of interest for a short-term power supply contract are the total power delivery, contract initiation time, and contract horizon. The contract initiation time is the time (hour) the contract execution commences. The contract horizon time is the total hours over which power has to be supplied. The total power delivery is the negotiated commitment of the delivery of pre-specified amounts of power. For example, the power producer can enter into a contract to supply 1000 MWh (total power delivery) over 9 hours (horizon time) beginning 8:00 AM on January 1st (initiation time). No hourly delivery constraints are assumed as long as the total power is delivered over the contract horizon. Furthermore, chemical batteries are assumed to smoothen minor fluctuations at the sub-hourly timescale.

Figure 11 shows the total power production in GWh aggregated across ERCOT for the two capacity allocation scenarios using the reanalysis data and the CKSTS generated simulations for different contract initiation times with a contract horizon of 12 hours for multiple days across the four seasons. Overall, the simulations bracket the underlying reanalysis data power production with no consistent bias. The simulation power production profiles for different contract initiations for different day across the four seasons show long tails, while the majority of the simulations have values near the data production values. Given multiple initiation times and days, the simulations accurately represent the underlying data generative process for this aggregated spatiotemporal metric.

Figure 12 shows the total power production in GWh aggregated across ERCOT for the two capacity allocation scenarios using the reanalysis data and the CKSTS generated simulations for different contract horizons with a contract initiation time of 8:00 AM for multiple days across the four seasons. Overall, the CKSTS generated simulations capture the underlying power production profiles in the reanalysis data. Furthermore, this holds for different contract period initializations and horizons across the year.

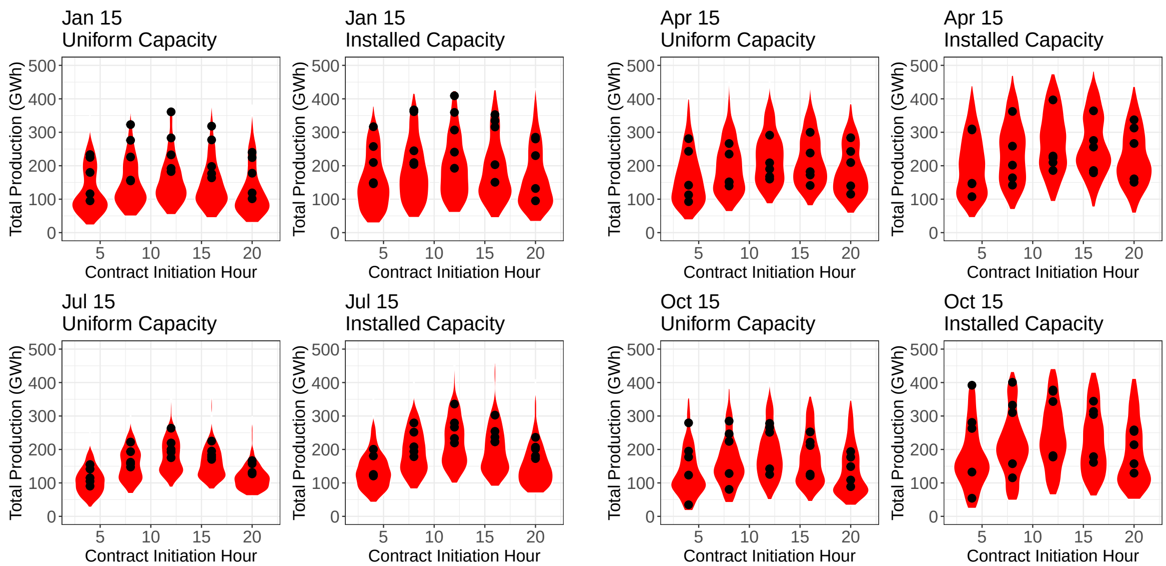

Figure 11: Energy production distribution profiles for different contract initiation times with a contract horizon of 12 hours for Uniform Capacity and Installed Capacity allocation scenarios. The initiation hours considered are 4 AM, 8 AM, 12 PM, 4 PM and 8 PM. The days considered are (A) January 15th (Winter), (B) April 15th (Spring), (c) July 15th (Summer), (D) October 15 (Fall). The black dotes denote the total power production during the contract for the data for each year and the red violin plots denote the values across the generated simulations.

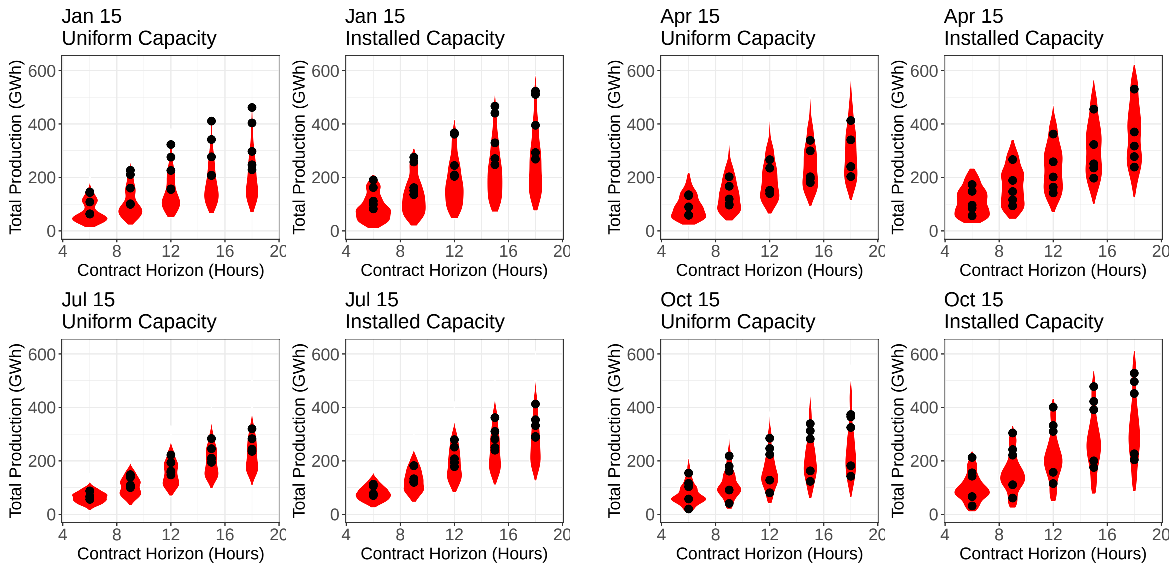

Figure 12: Energy production distribution profiles for different contract horizons, with a contract initiation time at 8:00 AM for Uniform Capacity and Installed Capacity allocation scenarios. The contract horizons considered are 6 hours, 9 hours, 12 hours, 15 hours and 18 hours. The days considered are (A) January 15th (Winter), (B) April 15th (Spring), (c) July 15th (Summer), (D) October 15 (Fall). The black dots denote the total power production during the contract for the data for each year, and the red violin plots denote the values across the generated simulations.

This example highlights the importance of modeling the spatial correlation structure of renewable generation sources. Furthermore, the manifestation of the spatially distributed generation risk is an interaction of the generative process and siting of the power generators. While we do not have control over the generative process (climate variability), our algorithm can be used for system analyses that seek to optimize some measure related to the expected reliability of renewable generation. A common trend across Figure 11 and 12 is that for the same contract horizon and initiation hour, the installed capacity allocation scenario leads to greater production than the uniform capacity scenario. By itself, this isn't surprising, since commercial renewable energy plants are located in regions with higher renewable generation potential. An interesting caveat is that while the total production is lower for the uniform capacity allocation scenario, its variation, as measured by the coefficient of variation, is also lower. This implies that the uniform capacity allocation, if utilized, has the potential to lower storage and battery usage in ERCOT. Optimization models that use CKSTS simulations could solve for the ideal profile of a target level of renewable energy generation with the highest reliability supported by the data for a specified budget constraint or equivalently to minimize installation cost for a target reliability level for the target production.

5 Discussion

The primary contribution of this paper is the introduction of the clustering-based k-nearest neighbor space-time simulator (CKSTS) algorithm and its application to the joint hourly wind-solar fields across the Texas Interconnection. The simulation skill of the CKSTS algorithm is analyzed by its ability to reproduce the marginal properties of wind and solar at each site, along with the field-level and cross-field spatiotemporal characteristics. The CKSTS generated simulations introduce a small bias in reproducing auto-correlation in both the aggregated field and at individual sites for the wind field. The magnitude of this bias is small and is attributed to the moving window used to capture seasonality in this study. An alternate formulation that considers seasonality more directly in the selection of the distance for the k-nearest neighbors could be explored. Overall, the generated simulations faithfully represent the underlying spatiotemporal properties of both wind and solar fields across ERCOT.

The CKSTS algorithm can be applied to any scenario generation problem where preserving the spatiotemporal dependence structure is of interest. We model the temporal dynamics using a Markovian process or through a time domain embedding informed by the time series. The primary difference between the CKSTS and the KSTS [47] is that the KSTS algorithm assumes complete homogeneity in the evolution of the dynamics, which is achieved by aggregating the resampling probabilities across all sites. The CKSTS is developed to avoid making this strong assumption of complete spatial homogeneity. The clustering helps identify spatial subsets that have similar evolution characteristics and separates them before simulating data for the next time step (Figure 3, Step 5).

The CKSTS is a non-parametric method, making no assumptions of the underlying density distributions of the modeled variables. Such a method is best suited for the application presented, since wind and solar are non-Gaussian distributions, with widely different data densities and spatiotemporal dependence structures dependent on seasonality. The CKSTS is a resampling scheme and can be considered a spatiotemporal bootstrap procedure. Different spatiotemporal kernels are used at each step to sample portions of the historical fields, with the resampling probabilities dependent on the kernel and distance metrics. The wind speed and solar radiation sequences at each site and aggregated across the region are different, even though the individual hourly values are resampled from the historical record. This limitation of resampling schemes (i.e., the inability of the simulations to include values not seen in the historical record) can be easily overcome. This is not a significant issue for either wind speeds or solar radiation, since the upper and lower ends of these distributions are bounded by practical concerns and recorded in the reanalysis datasets. Extrapolations to unseen values in the dataset can be achieved by fitting a parametric or non-parametric marginal probability distribution to each time series. Furthermore, marginal distributions can also be fit for each calendar hour/day with a penalization function that smooths seasonal variation in the parameters of the distribution being fit. Thereafter, if the rank of the selected nearest neighbor candidate is j, then the estimate based on the cumulative density distribution $F(x)$ is j/(n+1), where n is the sample size [72]. Overall, this extrapolation procedure does not change the basic structure of the CKSTS algorithm and allows for extrapolated values if required.

5.1 Next steps

The CKSTS algorithm and the generated simulations have additional applications in power system modeling studies. Generation/Capacity Expansion Models are optimization procedures that identify the least cost mix of generation resources and transmission infrastructure given governmental policies, constraints on emissions, economic goals, fuel prices, electricity demand projections, and technological advancements [73; 74]. These models are used for long-term energy system planning and analysis across large domains (i.e., sub-regional or national). The use of CKSTS simulations in capacity expansion models would involve using the models in a stochastic optimization setting. Zakaria et al. review stochastic optimization and uncertainty modeling for renewable energy applications [75]. Such models help reduce the error induced by the use of limited data (representative periods) [76] and in scenarios with a high share of renewables [77].

Furthermore, the CKSTS generated simulations can be used in stochastic unit commitment and economic dispatch models [78; 79]. In most cases, these models have a pre-specified generation, storage, and transmission capacity and do not model the evolution of these resources. While the CKSTS generated simulations can be incorporated in stochastic unit commitment formulations utilizing scenario selection, additional temporal granularity of the simulations (sub-hourly to 5 minutes) is required.

Data Availability

All code and data used for this study is publicly available at the GitHub repository `https://github.com/yashamonkar/CKSTS`.

Acknowledgments

The work described in this paper was partially supported by InnoHK initiative, The Government of the HKSAR, and Laboratory for AI-Powered Financial Technologies. Y.A. acknowledges support from the Cheung-Kong Innovation Doctoral Fellowship.

References

[1] California Legislative Information, "Senate Bill -100 California Renewables Portfolio Standard Program: emissions of greenhouse gases.," 2018.

[2] J. Deyette, "States March toward 100% Clean Energy–Who's Next?," Aug. 2019. Section: Energy.

[3] European Comission, "REGULATION OF THE EUROPEAN PARLIAMENT AND OF THE COUNCIL establishing the framework for achieving climate neutrality and amending Regulation (EU) 2018/1999 (European Climate Law)," 2020.

[4] New York State Legislatur, "New York's Climate Leadership and Community Protection Act (CLCPA)," 2019. https://climate.ny.gov/.

[5] International Renewable Energy Agency, "Renewable Power Generation Costs in 2019," tech. rep., 2020.

[6] NERC, "2012 State of Reliability," tech. rep., North American Electric Reliability Corporation, 2012.

[7] J. Doss-Gollin, Y. Amonkar, K. Schmeltzer, and D. Cohan, "Improving the Representation of Climate Risks in Long-Term Electricity Systems Planning: a Critical Review," *Current Sustainable/Renewable Energy Reports*, Aug. 2023.

[8] Y. Amonkar, J. Doss-Gollin, D. J. Farnham, V. Modi, and U. Lall, "Differential effects of climate change on average and peak demand for heating and cooling across the contiguous USA," *Communications Earth & Environment*, vol. 4, pp. 1–9, Nov. 2023. Publisher: Nature Publishing Group.

[9] NERC, "Resource Adequacy," 2023.

[10] J. Doss-Gollin, D. J. Farnham, U. Lall, and V. Modi, "How unprecedented was the February 2021 Texas cold snap?," *Environmental Research Letters*, vol. 16, p. 064056, June 2021. Publisher: IOP Publishing.

[11] ERCOT, "Monthly Outlook for Resource Adequacy (MORA) Reporting Month: July 2024," tech. rep., May 2024.

[12] ERCOT, "Seasonal Assessment of Resource Adequacy for the ERCOT Region (SARA) Fall 2023," tech. rep., 2023.

[13] NERC, "2023 Long-Term Reliability Assessment," tech. rep., Dec. 2023.

[14] S. Sundar, M. T. Craig, A. E. Payne, D. J. Brayshaw, and F. Lehner, "Meteorological drivers of resource adequacy failures in current and high renewable Western U.S. power systems," *Nature Communications*, vol. 14, p. 6379, Oct. 2023. Publisher: Nature Publishing Group.

[15] P. T. Brown, D. J. Farnham, and K. Caldeira, "Meteorology and climatology of historical weekly wind and solar power resource droughts over western North America in ERA5," *SN Applied Sciences*, vol. 3, p. 814, Sept. 2021.

[16] Y. Amonkar, J. Doss-Gollin, and U. Lall, "Compound Climate Risk: Diagnosing Clustered Regional Flooding at Inter-Annual and Longer Time Scales," *Hydrology*, vol. 10, p. 67, Mar. 2023. Number: 3 Publisher: Multidisciplinary Digital Publishing Institute.

[17] L. Bonnafous and U. Lall, "Space-time clustering of climate extremes amplify global climate impacts, leading to fat-tailed risk," *Natural Hazards and Earth System Sciences*, vol. 21, pp. 2277–2284, Aug. 2021. Publisher: Copernicus GmbH.

[18] D. S. Kirschen and G. Strbac, *Fundamentals of Power System Economics*. John Wiley & Sons, Sept. 2018. Google-Books-ID: I9hhDwAAQBAJ.

[19] S. Stoft, T. Belden, C. Goldman, and S. Pickle, "Primer on electricity futures and other derivatives," Tech. Rep. LBNL-41098, Lawrence Berkeley National Lab., Environmental Energy Technologies Div., Berkeley, CA (United States), 1998.

[20] M. Shahidehpour and M. Alomoush, *Restructured Electrical Power Systems: Operation: Trading, and Volatility*. Boca Raton: CRC Press, Jan. 2017.

[21] T. Couture and Y. Gagnon, “An analysis of feed-in tariff remuneration models: Implications for renewable energy investment,” *Energy Policy*, vol. 38, pp. 955–965, Feb. 2010.

[22] P. Rövekamp, M. Schöpf, F. Wagon, M. Weibelzahl, and G. Fridgen, “Renewable electricity business models in a post feed-in tariff era,” *Energy*, vol. 216, p. 119228, Feb. 2021.

[23] S. Collins, P. Deane, B. Ó Gallachóir, S. Pfenninger, and I. Staffell, “Impacts of Inter-annual Wind and Solar Variations on the European Power System,” *Joule*, vol. 2, pp. 2076–2090, Oct. 2018.

[24] J. A. Dowling, K. Z. Rinaldi, T. H. Ruggles, S. J. Davis, M. Yuan, F. Tong, N. S. Lewis, and K. Caldeira, “Role of Long-Duration Energy Storage in Variable Renewable Electricity Systems,” *Joule*, vol. 4, pp. 1907–1928, Sept. 2020.

[25] D. S. Wilks, “Use of stochastic weathergenerators for precipitation downscaling,” *WIREs Climate Change*, vol. 1, no. 6, pp. 898–907, 2010.

[26] P. Ailliot, D. Allard, V. Monbet, and P. Naveau, “Stochastic weather generators: an overview of weather type models,” *Journal de la société française de statistique*, vol. 156, no. 1, pp. 101–113, 2015.

[27] Y. Chen, Y. Wang, D. Kirschen, and B. Zhang, “Model-Free Renewable Scenario Generation Using Generative Adversarial Networks,” *IEEE Transactions on Power Systems*, vol. 33, pp. 3265–3275, May 2018. Conference Name: IEEE Transactions on Power Systems.

[28] W. B. Powell and S. Meisel, “Tutorial on Stochastic Optimization in Energy—Part I: Modeling and Policies,” *IEEE Transactions on Power Systems*, vol. 31, pp. 1459–1467, Mar. 2016. Conference Name: IEEE Transactions on Power Systems.

[29] W. B. Powell and S. Meisel, “Tutorial on Stochastic Optimization in Energy—Part II: An Energy Storage Illustration,” *IEEE Transactions on Power Systems*, vol. 31, pp. 1468–1475, Mar. 2016. Conference Name: IEEE Transactions on Power Systems.

[30] I. Goodfellow, J. Pouget-Abadie, M. Mirza, B. Xu, D. Warde-Farley, S. Ozair, A. Courville, and Y. Bengio, “Generative adversarial networks,” *Communications of the ACM*, vol. 63, pp. 139–144, Oct. 2020.

[31] Y. Chen, X. Wang, and B. Zhang, “An Unsupervised Deep Learning Approach for Scenario Forecasts,” in *2018 Power Systems Computation Conference (PSCC)*, pp. 1–7, June 2018.

[32] C. Jiang, Y. Mao, Y. Chai, M. Yu, and S. Tao, “Scenario Generation for Wind Power Using Improved Generative Adversarial Networks,” *IEEE Access*, vol. 6, pp. 62193–62203, 2018. Conference Name: IEEE Access.

[33] J. Sohl-Dickstein, E. Weiss, N. Maheswaranathan, and S. Ganguli, “Deep Unsupervised Learning using Nonequilibrium Thermodynamics,” in *Proceedings of the 32nd International Conference on Machine Learning*, pp. 2256–2265, PMLR, June 2015. ISSN: 1938-7228.

[34] X. Dong, Z. Mao, Y. Sun, and X. Xu, "Short-Term Wind Power Scenario Generation Based on Conditional Latent Diffusion Models," *IEEE Transactions on Sustainable Energy*, vol. 15, pp. 1074–1085, Apr. 2024. Conference Name: IEEE Transactions on Sustainable Energy.

[35] C. Xu, Y. Dai, P. Xu, T. Gao, and J. Zhang, "Wind Power Scenario Generation Based on Denoising Diffusion Probabilistic Model," in *2023 IEEE International Conference on Systems, Man, and Cybernetics (SMC)*, pp. 4525–4529, Oct. 2023. ISSN: 2577-1655.

[36] S. Li, C. Xu, L. Wei, R. Li, and X. Ai, "Scenario Generation of Renewable Energy Based on Improved Diffusion Model," in *2023 IEEE Sustainable Power and Energy Conference (iSPEC)*, pp. 1–7, Nov. 2023. ISSN: 2837-522X.

[37] S. Banerjee, B. P. Carlin, and A. E. Gelfand, *Hierarchical Modeling and Analysis for Spatial Data*. New York: Chapman and Hall/CRC, 2 ed., June 2014.

[38] Yufei Su, J. D. Kern, P. M. Reed, and G. W. Characklis, "Compound hydrometeorological extremes across multiple timescales drive volatility in California electricity market prices and emissions," *Applied Energy*, vol. 276, p. 115541, Oct. 2020.

[39] J. Després, S. Mima, A. Kitous, P. Criqui, N. Hadjsaid, and I. Noirot, "Storage as a flexibility option in power systems with high shares of variable renewable energy sources: a POLES-based analysis," *Energy Economics*, vol. 64, pp. 638–650, May 2017.

[40] M. Beaudin, H. Zareipour, A. Schellenberglabe, and W. Rosehart, "Energy storage for mitigating the variability of renewable electricity sources: An updated review," *Energy for Sustainable Development*, vol. 14, pp. 302–314, Dec. 2010.

[41] U. Ehret, E. Zehe, V. Wulfmeyer, K. Warrach-Sagi, and J. Liebert, "HESS Opinions "Should we apply bias correction to global and regional climate model data?"," *Hydrology and Earth System Sciences*, vol. 16, pp. 3391–3404, Sept. 2012. Publisher: Copernicus GmbH.

[42] S. Yakowitz, "Nearest-Neighbour Methods for Time Series Analysis," *Journal of Time Series Analysis*, vol. 8, no. 2, pp. 235–247, 1987.

[43] M. Karlsson and S. Yakowitz, "Nearest-neighbor methods for nonparametric rainfall-runoff forecasting," *Water Resources Research*, vol. 23, no. 7, pp. 1300–1308, 1987. _eprint: https://agupubs.onlinelibrary.wiley.com/doi/pdf/10.1029/WR023i007p01300.

[44] E. Fix and J. L. Hodges, "Discriminatory Analysis. Nonparametric Discrimination: Consistency Properties," *International Statistical Review / Revue Internationale de Statistique*, vol. 57, no. 3, pp. 238–247, 1989. Publisher: [Wiley, International Statistical Institute (ISI)].

[45] U. Lall and A. Sharma, "A Nearest Neighbor Bootstrap For Resampling Hydrologic Time Series," *Water Resources Research*, vol. 32, no. 3, pp. 679–693, 1996.

[46] B. Rajagopalan and U. Lall, "A k-nearest-neighbor simulator for daily precipitation and other weather variables," *Water Resources Research*, vol. 35, no. 10, pp. 3089–3101, 1999. _eprint: https://agupubs.onlinelibrary.wiley.com/doi/pdf/10.1029/1999WR900028.

[47] Y. Amonkar, D. J. Farnham, and U. Lall, “A k-nearest neighbor space-time simulator with applications to large-scale wind and solar power modeling,” *Patterns*, vol. 3, p. 100454, Mar. 2022.

[48] H. D. I. Abarbanel and M. B. Kennel, “Local false nearest neighbors and dynamical dimensions from observed chaotic data,” *Physical Review E*, vol. 47, pp. 3057–3068, May 1993. Publisher: American Physical Society.

[49] M. B. Kennel, R. Brown, and H. D. I. Abarbanel, “Determining embedding dimension for phase-space reconstruction using a geometrical construction,” *Physical Review A*, vol. 45, pp. 3403–3411, Mar. 1992. Publisher: American Physical Society.

[50] Electric Reliability Council of Texas, “About ERCOT,” 2021. http://www.ercot.com/about.

[51] US EIA, “Form EIA-860,” June 2023.

[52] US EIA, “Solar capacity additions are changing the shape of daily electricity supply in Texas - U.S. Energy Information Administration (EIA),” Apr. 2024.

[53] H. Hersbach, B. Bell, P. Berrisford, S. Hirahara, A. Horányi, J. Muñoz-Sabater, J. Nicolas, C. Peubey, R. Radu, D. Schepers, A. Simmons, C. Soci, S. Abdalla, X. Abellan, G. Balsamo, P. Bechtold, G. Biavati, J. Bidlot, M. Bonavita, G. D. Chiara, P. Dahlgren, D. Dee, M. Diamantakis, R. Dragani, J. Flemming, R. Forbes, M. Fuentes, A. Geer, L. Haimberger, S. Healy, R. J. Hogan, E. Hólm, M. Janisková, S. Keeley, P. Laloyaux, P. Lopez, C. Lupu, G. Radnoti, P. d. Rosnay, I. Rozum, F. Vamborg, S. Villaume, and J.-N. Thépaut, “The ERA5 global reanalysis,” *Quarterly Journal of the Royal Meteorological Society*, vol. 146, no. 730, pp. 1999–2049, 2020.

[54] P. E. Bett and H. E. Thornton, “The climatological relationships between wind and solar energy supply in Britain,” *Renewable Energy*, vol. 87, pp. 96–110, Mar. 2016.

[55] T. Caliński and J. Harabasz, “A dendrite method for cluster analysis,” *Communications in Statistics*, vol. 3, pp. 1–27, Jan. 1974.

[56] J. A. Hartigan and M. A. Wong, “Algorithm AS 136: A K-Means Clustering Algorithm,” *Journal of the Royal Statistical Society. Series C (Applied Statistics)*, vol. 28, no. 1, pp. 100–108, 1979. Publisher: [Wiley, Royal Statistical Society].

[57] S. C. Johnson, “Hierarchical clustering schemes,” *Psychometrika*, vol. 32, pp. 241–254, Sept. 1967.

[58] P. Drineas, A. Frieze, R. Kannan, S. Vempala, and V. Vinay, “Clustering in large graphs and matrices,” in *Proceedings of the tenth annual ACM-SIAM symposium on Discrete algorithms*, SODA ’99, (USA), pp. 291–299, Society for Industrial and Applied Mathematics, Jan. 1999.

[59] A. K. Jain, “Data clustering: 50 years beyond K-means,” *Pattern Recognition Letters*, vol. 31, pp. 651–666, June 2010.

[60] M. Meilă, “Comparing Clusterings by the Variation of Information,” in *Learning Theory and Kernel Machines* (B. Schölkopf and M. K. Warmuth, eds.), Lecture Notes in Computer Science, (Berlin, Heidelberg), pp. 173–187, Springer, 2003.

[61] A. Banerjee, S. Merugu, I. Dhillon, and J. Ghosh, "Clustering with Bregman Divergences," in *Proceedings of the 2004 SIAM International Conference on Data Mining*, pp. 234–245, Society for Industrial and Applied Mathematics, Apr. 2004.

[62] J. H. Ward, "Hierarchical Grouping to Optimize an Objective Function," *Journal of the American Statistical Association*, vol. 58, pp. 236–244, Mar. 1963.

[63] F. Murtagh and P. Legendre, "Ward's Hierarchical Clustering Method: Clustering Criterion and Agglomerative Algorithm," *Journal of Classification*, vol. 31, pp. 274–295, Oct. 2014. arXiv:1111.6285 [cs, stat].

[64] G. W. Milligan and M. C. Cooper, "An examination of procedures for determining the number of clusters in a data set," *Psychometrika*, vol. 50, pp. 159–179, June 1985.

[65] P. J. Rousseeuw, "Silhouettes: A graphical aid to the interpretation and validation of cluster analysis," *Journal of Computational and Applied Mathematics*, vol. 20, pp. 53–65, Nov. 1987.

[66] R. L. Thorndike, "Who belongs in the family?," *Psychometrika*, vol. 18, pp. 267–276, Dec. 1953.

[67] J. C. Dunn, "Well-Separated Clusters and Optimal Fuzzy Partitions," *Journal of Cybernetics*, vol. 4, pp. 95–104, Jan. 1974.

[68] D. L. Davies and D. W. Bouldin, "A Cluster Separation Measure," *IEEE Transactions on Pattern Analysis and Machine Intelligence*, vol. PAMI-1, pp. 224–227, Apr. 1979. Conference Name: IEEE Transactions on Pattern Analysis and Machine Intelligence.

[69] X. Xie and G. Beni, "A validity measure for fuzzy clustering," *IEEE Transactions on Pattern Analysis and Machine Intelligence*, vol. 13, pp. 841–847, Aug. 1991. Conference Name: IEEE Transactions on Pattern Analysis and Machine Intelligence.

[70] U. Maulik and S. Bandyopadhyay, "Performance evaluation of some clustering algorithms and validity indices," *IEEE Transactions on Pattern Analysis and Machine Intelligence*, vol. 24, pp. 1650–1654, Dec. 2002. Conference Name: IEEE Transactions on Pattern Analysis and Machine Intelligence.

[71] H. Abdi and L. J. Williams, "Principal component analysis," *WIREs Computational Statistics*, vol. 2, no. 4, pp. 433–459, 2010.

[72] L. Makkonen, "Bringing Closure to the Plotting Position Controversy," *Communications in Statistics - Theory and Methods*, vol. 37, pp. 460–467, Jan. 2008. Publisher: Taylor & Francis _eprint: https://doi.org/10.1080/03610920701653094.

[73] E. Boyd, "Power Sector Modeling 101.," Feb. 2016.

[74] I. Chernyakhovskiy, M. Joshi, and A. Rose, "Power System Planning: Advancements in Capacity Expansion Modeling," Tech. Rep. NREL/FS-5C00-80192, National Renewable Energy Lab. (NREL), Golden, CO (United States), Aug. 2021.

[75] A. Zakaria, F. B. Ismail, M. S. H. Lipu, and M. A. Hannan, "Uncertainty models for stochastic optimization in renewable energy applications," *Renewable Energy*, vol. 145, pp. 1543–1571, Jan. 2020.

[76] L. Reichenberg and F. Hedenus, "The error induced by using representative periods in capacity expansion models: system cost, total capacity mix and regional capacity mix," *Energy Systems*, Sept. 2022.

[77] S. Backe, M. Ahang, and A. Tomasgard, "Stable stochastic capacity expansion with variable renewables: Comparing moment matching and stratified scenario generation sampling," *Applied Energy*, vol. 302, p. 117538, Nov. 2021.

[78] M. Asensio and J. Contreras, "Stochastic Unit Commitment in Isolated Systems With Renewable Penetration Under CVaR Assessment," *IEEE Transactions on Smart Grid*, vol. 7, pp. 1356–1367, May 2016. Conference Name: IEEE Transactions on Smart Grid.

[79] M. Håberg, "Fundamentals and recent developments in stochastic unit commitment," *International Journal of Electrical Power & Energy Systems*, vol. 109, pp. 38–48, July 2019.

Supplementary Materials

Hyper-Parameter Selection

Resampling Kernel Function (p_j)

The resampling kernel used by Lall and Sharma (1996) is utilized in this study. The selected kernel has the property of decreasing monotonically with distance, where the kernel shape and bandwidth varies with the local sampling density. Overall, the kernel is implicitly adaptive to the dimension of the selected state space by means of the distance calculations. Furthermore, the resampling weights(p_j) are computed only once and stored, reducing computation requirements and time. Other options for the kernel include a uniform kernel ($p_j = 1/k$) or a power kernel based on the distances of the k neighbors. Lall and Sharma (1996) provide details on the behavior of the kernel for bounded data, in the boundary region, and comparison of the selected kernel to a uniform kernel.

Number of neighbors (k) and State Space order (m)

Following Lall and Sharma (1996), we have selected the number of neighbors (k) to be $k = n^{0.5}$, where is n is the total number of neighbor candidates. This ad-hoc choice is popular in the k-nearest neighbor algorithm literature, with the algorithm displaying low sensitivity around this value. Another method that can be used to select the number of neighbors (k) and state space order (m) involves criterion that minimize the mean squared error in forecast. The generalized cross validation (GCV) score was suggested to select k and m (Lall and Sharma (1996)). The selected number of nearest neighbors k and the order of the feature vector m are the ones which minimize the GCV score, which is given by

$$GCV = \frac{\sum_{i=1}^{n} e_i^2/n}{\left(1 - \frac{1}{\sum_{j=1}^{k} 1/j}\right)^2}$$

where, e_i is the forecast error at point i for the model fit to all the data without it and n is the total number of points. The selection of these parameters by GCV is most appropriate if the model errors e_i are normally distributed or if the variables are transformed such that model errors are normally distributed. Non-normality of the errors may lead to suboptimal choice of *k* and *m* with respect to its conditional mean and variance. Another method to select the model lags in the feature vector is the false nearest neighbors algorithm, which determines the embedding dimension for the process (Kennel et al (1992)).

Scaling weights (w)

The simplest selection choice for the weights w, which weigh the Euclidean distance of the selected lags, m is to be specified *a priori* with uniform values. The weights can also be selected such that they minimize the forecast error in the least squares sense when used in a knn regression setup (Yakowitz and Karlsson (1987)). An alternate adaptive strategy is to compute scaling weights (w) for the knn resampling approach such that they are the regression coefficients of the selected external predictors from a parametric regression model (Souza Filho et al. (2003)).

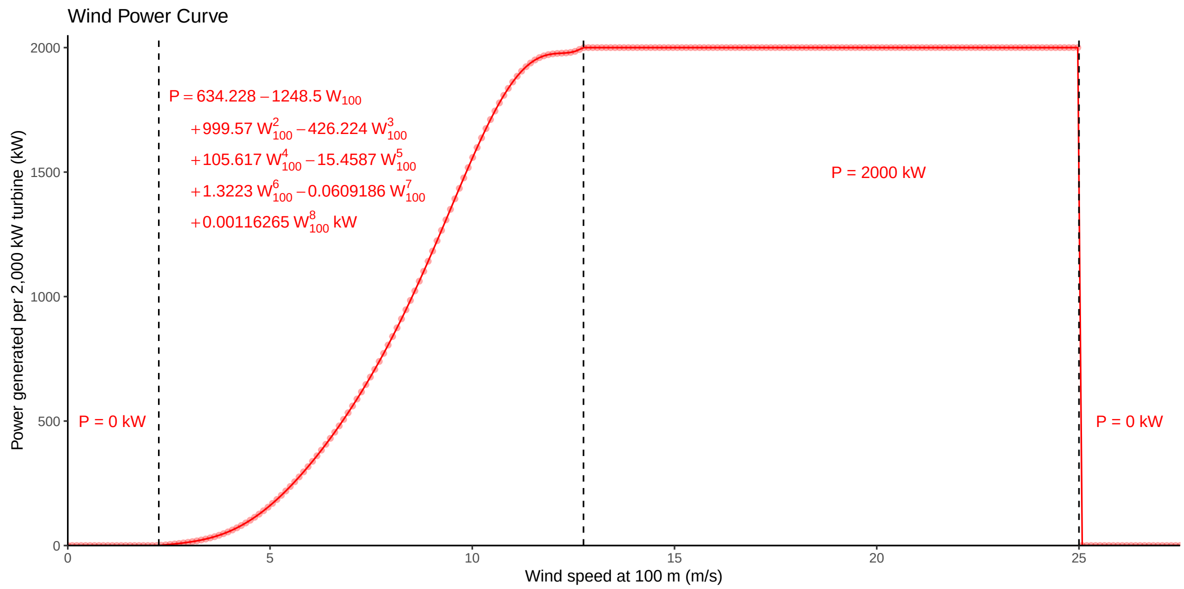

Figure S1: Wind Power Curve for a V90-2.0MW Vestas turbine.

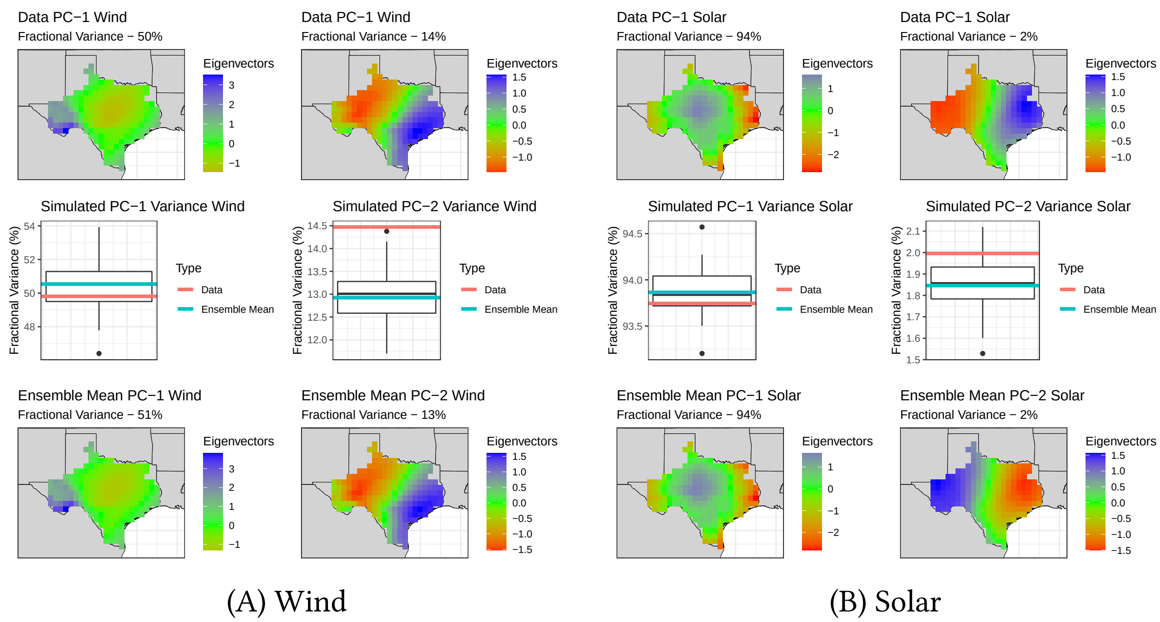

Figure S2: Principal component analysis of the (A) wind and (B) solar fields. The top row denotes the reanalysis data PC-1 and PC-2 respectively. The middle row denotes the variance (eigenvalues) associated with PC-1 and PC-2. The red and blue line denotes the reanalysis data and median simulation variance. The boxplot denotes the spread in the variance among the generated 48 simulations.The bottom row denotes the median of the simulations PC-1 and PC-2 respectively. The colors for the top and the bottom row correspond to eigenvectors of the PCs.

5.1.1 Moments of the distribution

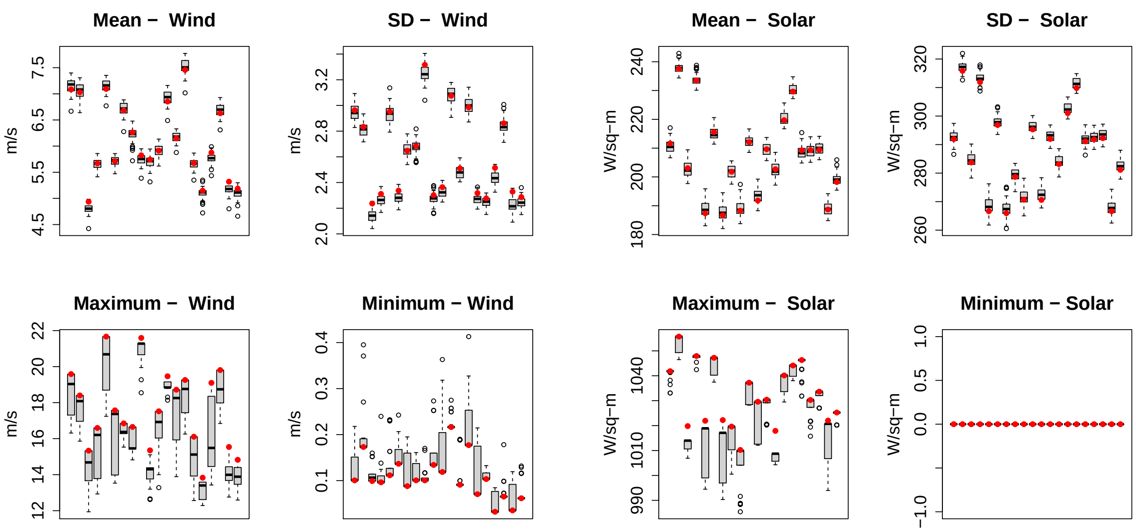

(a) Wind (b) Solar

Figure S3: Simulation skill assessments for individual sites in the wind and solar fields for the generated simulations. (A) Wind. (B) Solar. For each sub-plot, we show the mean (top-left), the standard deviation (top-right), the maximum (bottom-left), and the minimum (bottom-right). Red dots denote the reanalysis data value, and box-plots denote the spread among the generated simulations.Each subplot includes results for 20 randomly selected grid points out of the 216 total grids.

5.1.2 Spatial cross-correlation

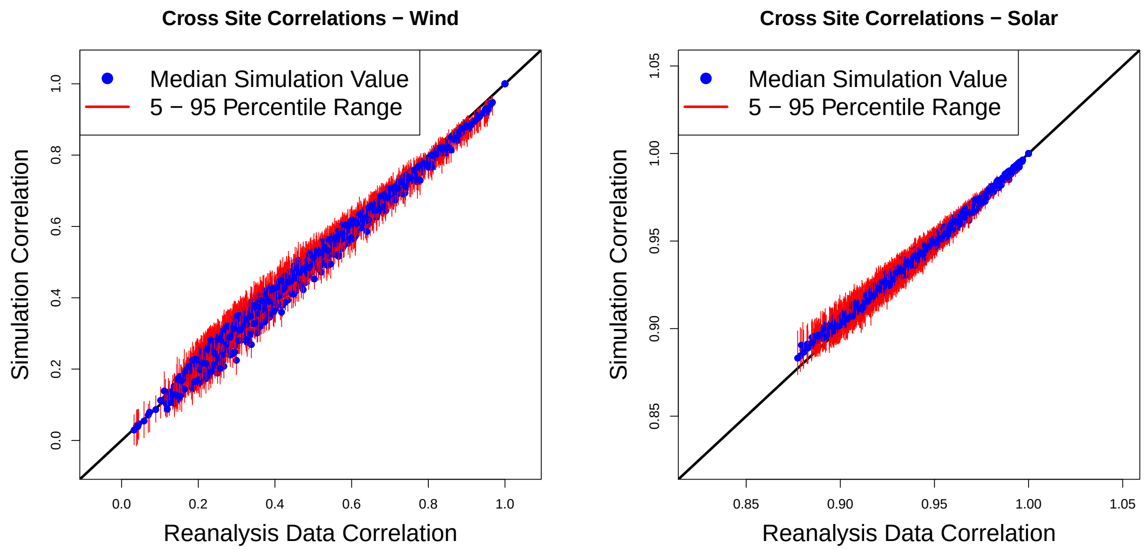

(A) Wind

(B) Solar

Figure S4: Simulation vs. reanalysis data cross-site correlation plots for individual fields. (A) Wind. (B) Solar. 40 grids out of 216 are randomly selected, and the 40 x 40 cross-correlation values are computed and plotted instead of the entire 216 x 216 correlation values. The correlations are computed using Pearson's method. The red lines denote the mid-90th (5th-95th) percentile range, and the blue dots denote the median value in the simulation spread.

5.1.3 Temporal auto-correlation

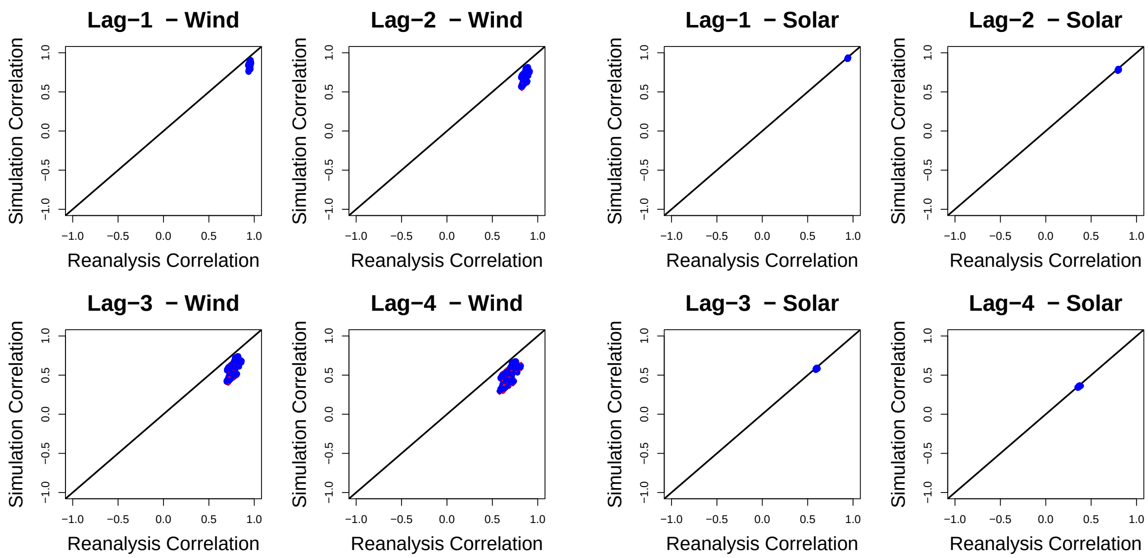

(A) Wind (B) Solar

Figure S5: Simulation vs. reanalysis data auto-correlation plots for lag 1,2,3, and 4 for all grid points. (A) Wind. (B) Solar. The red lines denote the mid-90th (5th-95th) percentile range, and the blue dots denote the median value in the simulation spread.

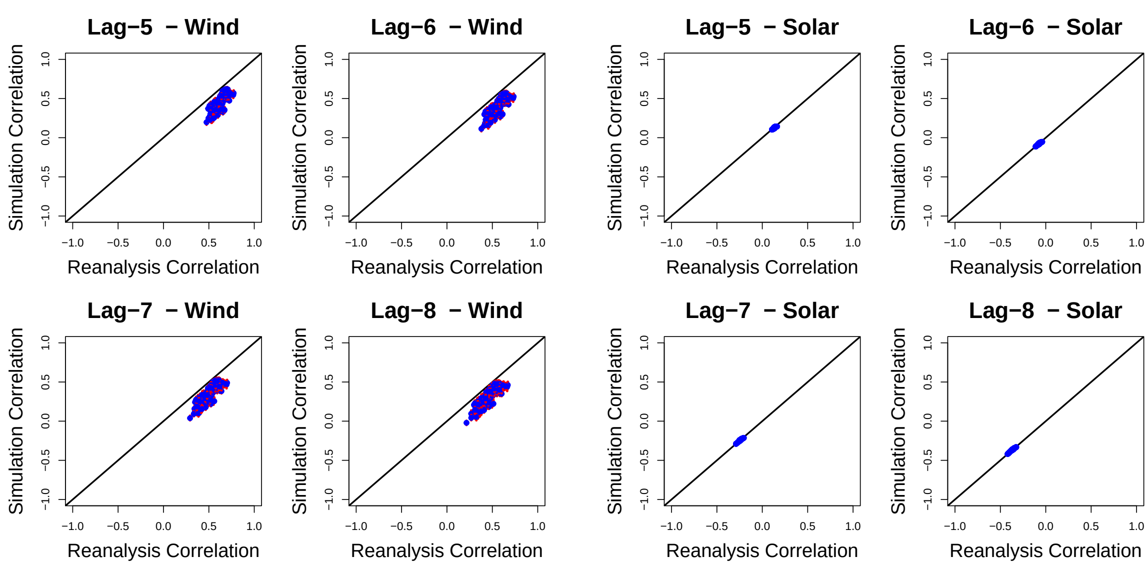

(A) Wind (B) Solar

Figure S6: Simulation vs. reanalysis data auto-correlation plots for lag 5,6,7, and 8 for all grid points. (A) Wind. (B) Solar. The red lines denote the mid-90th (5th-95th) percentile range, and the blue dots denote the median value in the simulation spread.

5.1.4 Density distribution

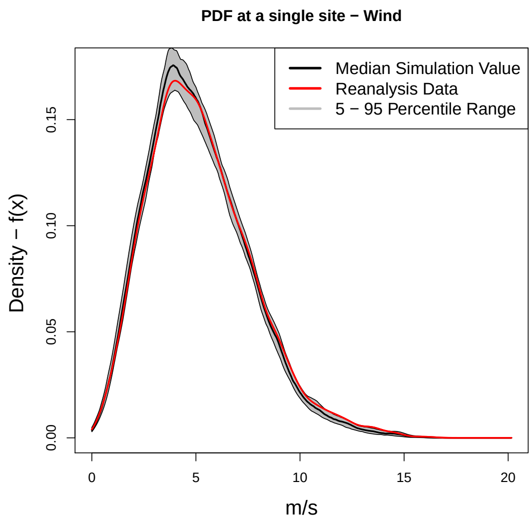

(A) Wind

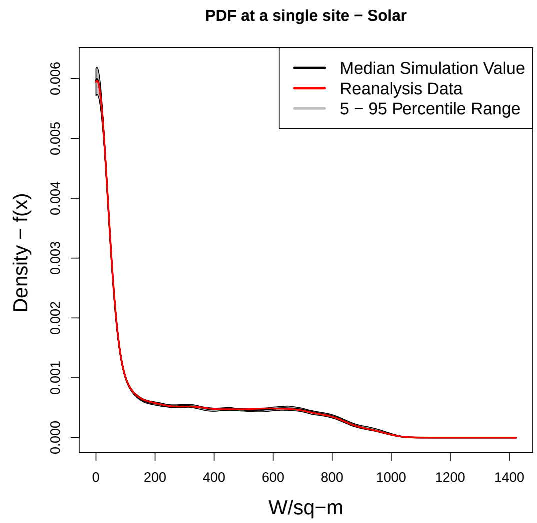

(B) Solar

Figure S7: Kernel density estimate / probability density function (PDF) plots for a single randomly selected grid for wind and solar. The red line denotes the reanalysis data probability density function for the selected site, and the black line denotes the median simulation density. The gray region is the mid 90th (5th-95th) percentile range of the simulation spread. The grid point is selected at random separately for both fields. (A) Wind. (B) Solar.

5.1.5 Quantiles

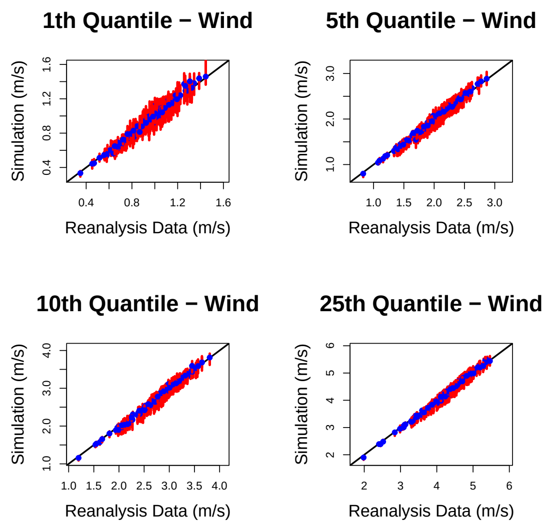

(A) Wind

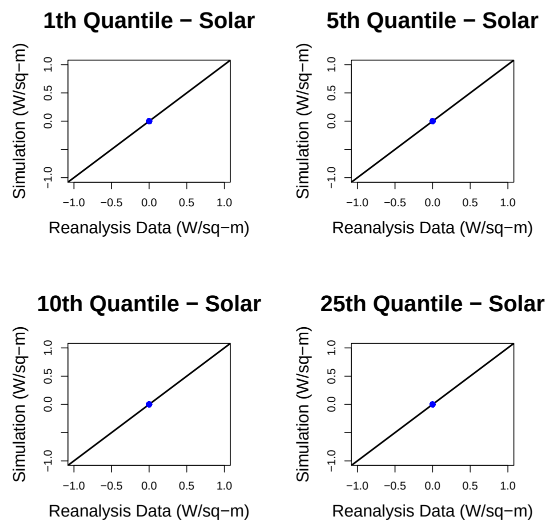

(B) Solar

Figure S8: Simulation vs. reanalysis data quantile plots for the 1st, 5th, 10th, 25th, percentiles. (A) Wind. (B) Solar. The plots denote the quantiles for all 216 grid points in the wind and solar fields. The red lines denote the mid 90th (5th-95th) percentile range, and the blue dots denote the median value in the simulation spread.

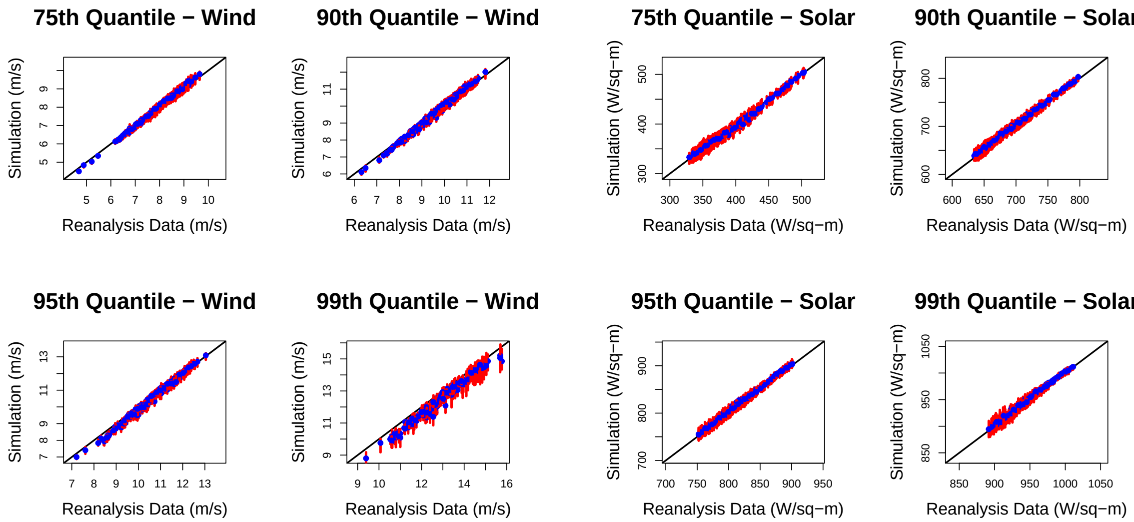

(A) Wind

(B) Solar

Figure S9: Simulation vs. reanalysis data quantile plots for the 75th, 90th, 95th, 99th, percentiles. (A) Wind. (B) Solar. The plots denote the quantiles for all 216 grid points in the wind and solar fields. The red lines denote the mid 90th (5th-95th) percentile range, and the blue dots denote the median value in the simulation spread.

5.1.6 Seasonality and diurnal cycle

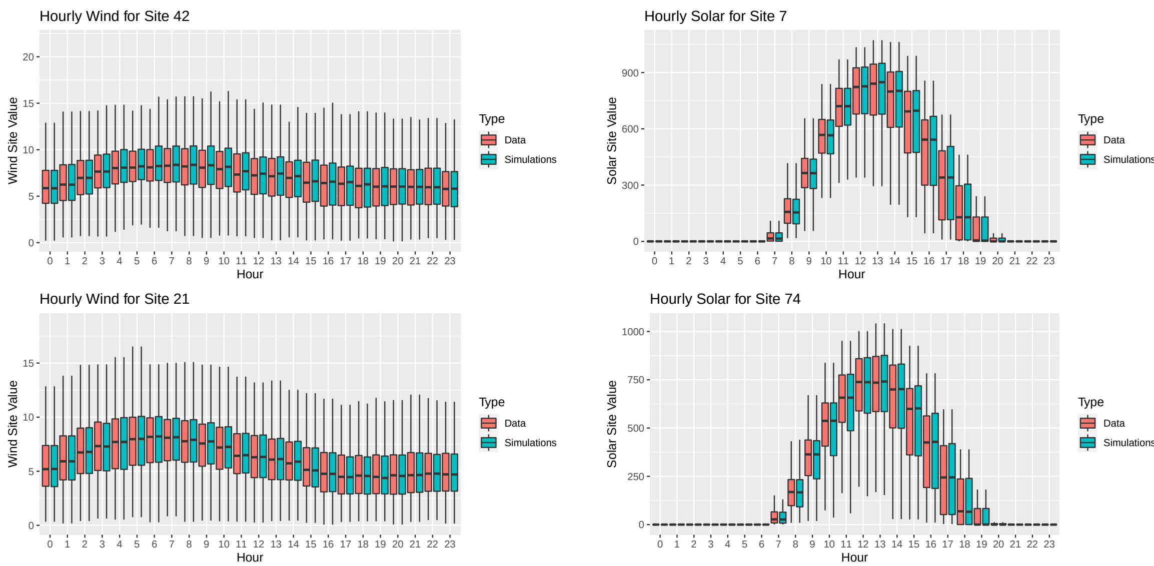

(A) Wind (B) Solar

Figure S10: Hourly distribution of the reanalysis data and simulations. The red and green boxplots denote the reanalysis data and simulations, respectively. (A) Wind. (B) Solar. Two grid points are randomly selected for wind and solar. The grids are selected at random separately. The hours are numbered with midnight being assigned 0.

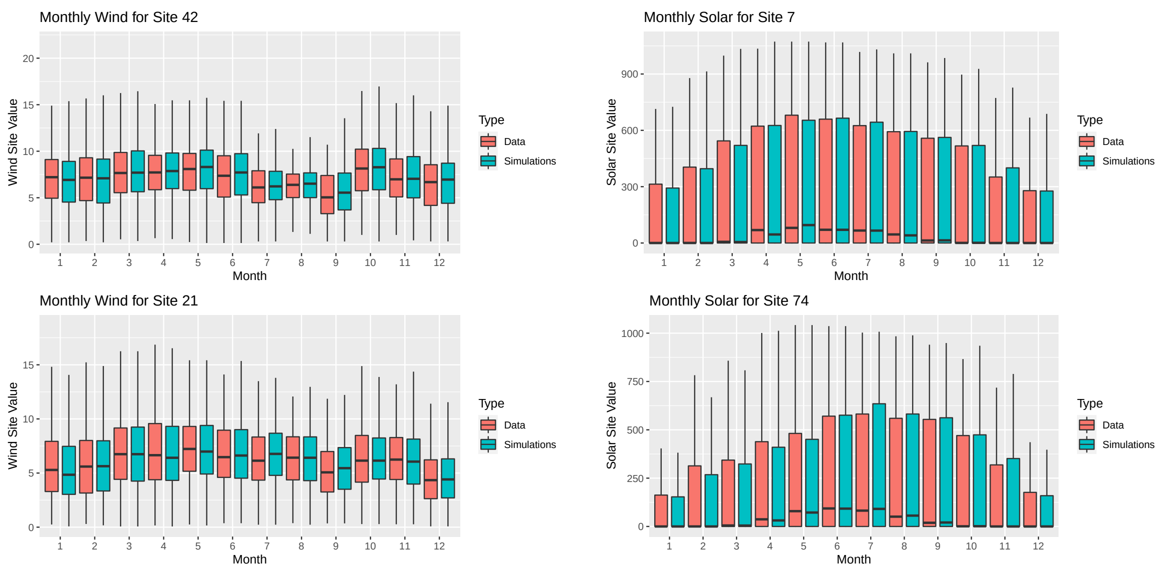

(A) Wind

(B) Solar

Figure S11: Seasonality / Monthly distribution of the reanalysis data and simulations. The red and green boxplots denote the reanalysis data and simulations, respectively. (A) Wind. (B) Solar. Two grid points are randomly selected for wind and solar. The grids are selected at random separately. Months are numbered in accordance with the Gregorian calendar

Supplementary Materials - References

1. Lall, Upmanu, and Ashish Sharma. "A nearest neighbor bootstrap for resampling hydrologic time series." Water resources research 32.3 (1996): 679-693.

2. Kennel, Matthew B., Reggie Brown, and Henry DI Abarbanel. "Determining embedding dimension for phase-space reconstruction using a geometrical construction." Physical review A 45.6 (1992): 3403.

3. Yakowitz, S., and M. Karlsson. "Nearest neighbor methods for time series, with application to rainfall/runoff prediction." Advances in the statistical sciences: Stochastic hydrology. Springer, Dordrecht, 1987. 149-160.

4. Souza Filho, Francisco Assis, and Upmanu Lall. "Seasonal to interannual ensemble streamflow forecasts for Ceara, Brazil: Applications of a multivariate, semiparametric algorithm." Water Resources Research 39.11 (2003).